This is a preprint, the final version is subject to change, of the American Mineralogist (MSA)
Cite as Authors (Year) Title. American Mineralogist, in press.
DOI: http://dx.doi.org/10.2138/am-2018-6124

Revision 2:
Crystal chemistry of martian minerals from Bradbury Landing through Naukluft Plateau, Gale crater, Mars

SHAUNNA M. MORRISON,[1,2*] ROBERT T. DOWNS,[1] DAVID F. BLAKE,[3] DAVID T. VANIMAN,[4] DOUGLAS W. MING,[5] ROBERT M. HAZEN,[2] ALLAN H. TREIMAN,[6] CHERIE N. ACHILLES,[1] ALBERT S. YEN,[7] RICHARD V. MORRIS,[5] ELIZABETH B. RAMPE,[5] THOMAS F. BRISTOW,[3] STEVE J. CHIPERA,[8] PHILIPPE C. SARRAZIN,[9] RALF GELLERT,[10] KIM V. FENDRICH,[11] JOHN MICHAEL MOROOKIAN,[7] JACK D. FARMER,[12] DAVID J. DES MARAIS,[3] AND PATRICIA I. CRAIG[6]

[1]UNIVERSITY OF ARIZONA, 1040 E 4TH ST, TUCSON, AZ, 85721 U.S.A.
[2]GEOPHYSICAL LABORATORY, CARNEGIE INSTITUTION, 5251 BROAD BRANCH RD NW, WASHINGTON, DC, 20015 U.S.A.
[3]NASA AMES RESEARCH CENTER, MOFFETT FIELD, CA 94035, U.S.A.
[4]PLANETARY SCIENCE INSTITUTE, 1700 E. FORT LOWELL, TUCSON, AZ 85719-2395, U.S.A.
[5]NASA JOHNSON SPACE CENTER, HOUSTON, TX, 77058 U.S.A.
[6]LUNAR AND PLANETARY INSTITUTE - USRA, 3600 BAY AREA BLVD, HOUSTON, TX 77058, U.S.A.
[7]JET PROPULSION LABORATORY, CALIFORNIA INSTITUTE OF TECHNOLOGY, 4800 OAK GROVE DRIVE, PASADENA, CA 91109, U.S.A.
[8]CHESAPEAKE ENERGY CORPORATION, 6100 N. WESTERN AVENUE, OKLAHOMA CITY, OK 73118, U.S.A.
[9]SETI INSTITUTE, MOUNTAIN VIEW, CA 94043 U.S.A.
[10]UNIVERSITY OF GUELPH, 50 STONE RD E, GUELPH, ON N1G 2W1, CANADA
[11]AMERICAN MUSEUM OF NATURAL HISTORY, NEW YORK, NY 10024, U.S.A.
[12]ARIZONA STATE UNIVERSITY, TEMPE, AZ, 85281 U.S.A.

ABSTRACT

Crystal chemical algorithms were used to estimate the chemical composition of selected mineral phases observed with the CheMin X-ray diffractometer onboard the NASA Curiosity rover in Gale crater, Mars. The sampled materials include two wind-blown soils, Rocknest and Gobabeb, six mudstones in the Yellowknife Bay formation (John Klein and Cumberland) and the Murray formation (Confidence Hills, Mojave2, and Telegraph Peak), as well as five sandstones, Windjana and the samples of the unaltered Stimson formation (Big Sky and Okoruso) and the altered Stimson formation (Greenhorn and Lubango). The major mineral phases observed with the CheMin instrument in the Gale crater include plagioclase, sanidine, $P2_1/c$ and $C2/c$ clinopyroxene, orthopyroxene, olivine, spinel, and alunite-jarosite group minerals. The plagioclase analyzed with CheMin has an overall estimated average of $An_{40(11)}$ with a range of $An_{30(8)}$ to $An_{63(6)}$. The soil samples, Rocknest and Gobabeb, have an average of $An_{56(8)}$ while the

This is a preprint, the final version is subject to change, of the American Mineralogist (MSA)
Cite as Authors (Year) Title. American Mineralogist, in press.
DOI: http://dx.doi.org/10.2138/am-2018-6124

Murray, Yellowknife Bay, unaltered Stimson, and altered Stimson formations have averages of $An_{38(2)}$, $An_{37(5)}$, $An_{45(7)}$ and $An_{35(6)}$, respectively. Alkali feldspar, specifically sanidine, average composition is $Or_{74(17)}$ with fully disordered Al/Si. Sanidine is most abundant in the Windjana sample (~26 wt % of the crystalline material) and is fully disordered with a composition of $Or_{87(5)}$. The $P2_1/c$ clinopyroxene, pigeonite, observed in Gale crater has a broad compositional range $\{[Mg_{0.95(12)\text{-}1.54(17)}Fe_{0.18(17)\text{-}1.03(9)}Ca_{0.00\text{-}0.28(6)}]_{\Sigma=2}Si_2O_6\}$ with an overall average of $Mg_{1.18(19)}Fe_{0.72(7)}Ca_{0.10(9)}Si_2O_6$. The soils have the lowest Mg and highest Fe compositions $[Mg_{0.95(5)}Fe_{1.02(7)}Ca_{0.03(4)}Si_2O_6]$ of all of the Gale samples. Of the remaining samples, those of the Stimson formation exhibit the highest Mg and lowest Fe [average = $Mg_{1.45(7)}Fe_{0.35(13)}Ca_{0.19(6)}Si_2O_6$]. Augite, $C2/c$ clinopyroxene, is detected in just three samples, the soil samples [average = $Mg_{0.92(5)}Ca_{0.72(2)}Fe_{0.36(5)}Si_2O_6$] and Windjana ($Mg_{1.03(7)}Ca_{0.75(4)}Fe_{0.21(9)}Si_2O_6$). Orthopyroxene was not detected in the soil samples and has an overall average composition of $Mg_{0.79(6)}Fe_{1.20(6)}Ca_{0.01(2)}Si_2O_6$ and a range of $[Mg_{0.69(7)\text{-}0.86(20)}Fe_{1.14(20)\text{-}1.31(7)}Ca_{0.00\text{-}0.04(4)}]_{\Sigma=2}Si_2O_6$, with Big Sky exhibiting the lowest Mg content $[Mg_{0.69(7)}Fe_{1.31(7)}Si_2O_6]$ and Okoruso exhibiting the highest $[Mg_{0.86(20)}Fe_{1.14(20)}Si_2O_6]$. Appreciable olivine was observed in only three of the Gale crater samples, the soils and Windjana. Assuming no Mn or Ca, the olivine has an average composition of $Mg_{1.19(12)}Fe_{0.81(12)}SiO_4$ with a range of 1.08(3) to 1.45(7) Mg apfu. The soil samples [average = $Mg_{1.11(4)}Fe_{0.89}SiO_4$] are significantly less magnesian than Windjana $[Mg_{1.35(7)}Fe_{0.65(7)}SiO_4]$. We assume magnetite ($Fe_3O_4$) is cation-deficient ($Fe_{3-x}\square_xO_4$) in Gale crater samples [average = $Fe_{2.83(5)}\square_{0.14}O_4$; range 2.75(5) to 2.90(5) Fe apfu], but we also report other plausible cation substitutions such as Al, Mg, and Cr that would yield equivalent unit-cell parameters. Assuming cation-deficient magnetite, the Murray formation [average = $Fe_{2.77(2)}\square_{0.23}O_4$] is noticeably more cation-deficient than the other Gale

samples analyzed by CheMin. Note that despite the presence of Ti-rich magnetite in martian meteorites, the unit-cell parameters of Gale magnetite do not permit significant Ti substitution. Abundant jarosite is found in only one sample, Mojave2; its estimated composition is $(K_{0.51(12)}Na_{0.49})(Fe_{2.68(7)}Al_{0.32})(SO_4)_2(OH)_6$. In addition to providing composition and abundances of the crystalline phases, we calculate the lower limit of the abundance of X-ray amorphous material and the composition thereof for each of the samples analyzed with CheMin. Each of the CheMin samples had a significant proportion of amorphous SiO_2, except Windjana which has 3.6 wt% SiO_2. Excluding Windjana, the amorphous materials have an SiO_2 range of 24.1 to 75.9 wt% and an average of 47.6 wt%. Windjana has the highest FeO_T (total Fe content calculated as FeO) at 43.1 wt%, but most of the CheMin samples also contain appreciable Fe, with an average of 16.8 wt%. With the exception of the altered Stimson formation samples, Greenhorn and Lubango, the majority of the observed SO_3 is concentrated in the amorphous component (average = 11.6 wt%). Furthermore, we provide average amorphous-component compositions for the soils and the Mount Sharp group formations, as well as the limiting element for each CheMin sample.

Keywords: Mars, Gale crater, Mars Science Laboratory, CheMin, X-ray diffraction, crystal chemistry, plagioclase, olivine, pyroxene, magnetite, jarosite, alunite.

INTRODUCTION

The NASA Mars Science Laboratory (MSL) rover, Curiosity, began exploring Gale crater, Mars in August 2012 with the primary goal of assessing the planet's past and present habitability (Grotzinger 2013). To meet this objective, Curiosity is equipped with an advanced suite of scientific instruments. Among these is the Chemistry and Mineralogy (CheMin) X-ray diffractometer (Blake et al. 2012), capable of determining the mineralogy of rocks and

This is a preprint, the final version is subject to change, of the American Mineralogist (MSA)
Cite as Authors (Year) Title. American Mineralogist, in press.
DOI: http://dx.doi.org/10.2138/am-2018-6124

unconsolidated sediments acquired by the rover's Sample Acquisition, Sample Processing and Handling (SA/SPaH) system (Anderson et al. 2012). As of June 2016, CheMin has measured 13 samples (2 scooped soils and 11 drilled sedimentary rocks) along Curiosity's traverse in Gale crater (Table 1). Prior to CheMin's definitive mineralogical analyses, Mars missions relied on spectral models, normative mineral calculations based on bulk sample chemical composition, or select Fe-bearing oxide phase or silicate phase and oxidation state identification by Mössbauer spectroscopy (e.g., Christensen et al. 2004a, 2004b; Clark et al. 2005; Morris et al. 2006, 2008; Ruff et al. 2008). These approaches provide important information, but cannot determine relative mineral abundance or crystal chemistry with the accuracy and precision of X-ray diffraction (XRD) and Rietveld refinement. Definitive mineralogy is critical to our understanding of early environments of formation and post-depositional diagenetic processes. Crystal-chemical analyses can provide additional detail about past martian conditions by providing estimates of cation distribution within a specific mineral or phase.

Curiosity is not equipped to directly measure the chemical composition of individual mineral phases within a multi-phase sample. However, CheMin produces XRD patterns from which each crystalline phase can be identified along with the unit-cell parameters of the major phases (Blake et al. 2012). It is important to note that zoning or variation in chemistry of a single phase is not readily detected with CheMin and, therefore, the unit-cell parameters obtained for a phase represent the average thereof. Unit-cell parameters vary with chemical composition as they respond to changes in atomic radii; therefore, measured unit-cell parameters provide quantitative mineral chemical composition (Morrison et al. 2017).

In this study, we present the methods used by the CheMin science team to calibrate XRD patterns, to estimate the chemical composition of the major mineral phases (Morrison et al.

This is a preprint, the final version is subject to change, of the American Mineralogist (MSA)
Cite as Authors (Year) Title. American Mineralogist, in press.
DOI: http://dx.doi.org/10.2138/am-2018-6124

2017), and, in conjunction with bulk elemental data from the Alpha Particle X-ray Spectrometer (APXS) (Campbell et al. 2012; Gellert et al. 2015; Thompson et al. 2016; O'Connell-Cooper 2017), to derive the composition of the amorphous components present in each sample. In addition, we describe a new procedure in which plagioclase feldspar is used as an internal standard to provide improved calibration of the instrument. This new "sample cell offset" calibration has resulted in updated unit-cell parameters and chemical composition of the phases reported in Rocknest (Bish et al. 2013; Blake et al. 2013; Dehouck et al. 2014), Yellowknife Bay (Treiman et al. 2014; Vaniman et al. 2014; Dehouck et al. 2014), and Kimberley (Treiman et al. 2016) formations. The data published herein and in Morris et al. (2016), Achilles et al. (2017), Rampe et al. (2017), and Yen et al. (2017) are the most up-to date and accurate unit-cell parameters for all samples analyzed with CheMin in Gale crater, Mars (Table 2). Additionally, since the publication of Morris et al. (2016), Achilles et al. (2017), Rampe et al. (2017), and Yen et al. (2017), we have further refined the crystal-chemical algorithms, as reported in Morrison et al. (2017), and, as a result, the chemical compositions presented here may differ slightly (within 1-sigma uncertainty) from those previously reported.

CheMin X-Ray Diffraction

The CheMin X-ray diffractometer produces diffraction patterns that identify minerals in unconsolidated sediments or drilled rock samples. Material is sieved to < 150 μm before delivery to one of the instrument's 27 reusable sample cells located within the interior of the rover (Fig. 1). The sample cells, positioned in pairs at the ends of tuning forks, hold the sample between two polymer (Kapton or Mylar) windows 175 μm apart (Fig. 2). A piezoelectric actuator drives the tuning fork at resonance, and the resulting vibration causes a convective flow of sample material through the collimated 70-μm diameter X-ray beam, thus randomizing grain orientations and

This is a preprint, the final version is subject to change, of the American Mineralogist (MSA)
Cite as Authors (Year) Title. American Mineralogist, in press.
DOI: http://dx.doi.org/10.2138/am-2018-6124

minimizing orientation effects. The instrument utilizes transmission geometry with a Co X-ray source (Kα1,2 av. λ = 1.7902758 Å). An X-ray sensitive charge-coupled device (CCD) collects two-dimensional (2D) XRD images over 10 to 40 hours of analysis. The CCD detector is operated in single-photon counting mode (the detector is read out sufficiently often that most pixels contain either no charge or charge derived from a single photon). When operated in this manner, the CCD can be used to measure the amount of charge generated by each photon (and hence its energy). Diffracted CoKα X-ray photons are identified by their energy and are summed to yield a 2D energy-discriminated CoKα diffraction pattern. The short sample-to-detector distance required for instrument miniaturization results in a 2θ resolution (≤ 0.30°) lower than that of a full-size laboratory diffractometer (~0.03° 2θ) (RRUFF.info). The CheMin team uses a modification of GSE_ADA software (Dera et al. 2013) to convert 2D images to 1-dimensional (1D) patterns with any necessary corrections for alignment bias. We use the Rietveld refinement method (Young 1993) in Materials Data Inc.'s JADE^{TM} software to determine abundances of all crystalline phases as well as unit-cell parameters of major crystalline phases (Table 2). FULLPAT analysis (Chipera and Bish 2002, 2013) yields the XRD-determined abundance of clay minerals and amorphous components.

Mineral unit-cell parameters, abundances, and compositions were reported earlier for the Rocknest soil (Bish et al. 2013; Blake et al. 2013), the Yellowknife Bay mudstones, John Klein and Cumberland (Treiman et al. 2014; Vaniman et al. 2014; Bristow et al. 2015), and the Windjana sandstone (Treiman et al. 2016). Subsequent to these publications, the CheMin team has increased the accuracy of 1D pattern refinement through additional instrument geometry corrections and refinement of 2D-to-1D parameters, the method for which is given in the

This is a preprint, the final version is subject to change, of the American Mineralogist (MSA)
Cite as Authors (Year) Title. American Mineralogist, in press.
DOI: http://dx.doi.org/10.2138/am-2018-6124

following section. Updated unit-cell parameters, abundances, and estimated chemical composition are shown here, and supersede those reported earlier (Table 2 and Tables 4-10).

SAMPLE CELL OFFSET CALIBRATION

The initial 2θ calibration was based on the measurement of a well-characterized beryl-quartz standard housed in one of CheMin's sample cells. On the basis of this measurement, the sample cell-to-CCD distance is calculated to be 18.5302 mm. When a sample is delivered from SA/SPaH, the CheMin wheel is rotated to the location of a specified reusable sample cell and clamped into place. The machining tolerance of the center of individual sample cells is ±50 μm, and this uncertainty accounts for the largest contribution to 2θ measurement error in the instrument (Fig. 2). The resulting deviation in the diffracting position, along with thermal expansion and contraction of the instrument and its components and grain motion effects within the sample cell, causes subtle shifts in 2θ resulting in a small systematic error in refined cell parameters and derived estimates of mineral composition.

In order to determine the offset distance for each sample cell, we developed a novel method using unit-cell parameters of Na-Ca plagioclase (<0.042 K apfu). Plagioclase is abundant in almost all CheMin martian samples measured to date, except Windjana. Published values for plagioclase unit-cell parameters (Table A1a; data table available in csv format at github.com/shaunnamm/regression-and-minimization) exhibit a large degree of internal consistency, especially between *c* and γ, over the range of cell parameters observed on Mars, as evidenced by the highly correlated linear trend in Figure 3a. Significant deviations from the terrestrial *c* versus γ trend are sometimes observed for CheMin-refined unit-cell parameters, such as those of Rocknest plotted on Figure 3a. In the absence of evidence to demonstrate that martian

This is a preprint, the final version is subject to change, of the American Mineralogist (MSA)
Cite as Authors (Year) Title. American Mineralogist, in press.
DOI: http://dx.doi.org/10.2138/am-2018-6124

177 plagioclase would produce a trend different from the Earth-derived relationship, we assume
178 plagioclase on Mars should follow terrestrial trends. According to Papike et al. (2009),
179 plagioclase/maskelynite in martian meteorites is close to the albite-anorthite join, and contains
180 little K (K_2O 0.04 to 2.11 wt%), Fe^{3+} (Fe_2O_3 0.2 to 1.1 wt%), and Mg (MgO 0 to 0.23 wt%).
181 Such small amounts of K, Fe and Mg will not cause the unit-cell parameters of plagioclase to
182 deviate from the anorthite-albite trend of Figure 3a outside its uncertainty (Morrison et al. 2017).
183 Therefore, the variation observed in CheMin unit-cell parameters cannot be attributed to the
184 small amounts of K, Fe, and Mg as reported in martian meteorites.

185 In order to calibrate the sample cell offset, we vary the sample-to-detector distance in the
186 GSE_ADA software to produce a set of diffraction patterns with the sample position moved
187 systematically over a range of +/- 45 μm. Subsequently, we perform Rietveld refinements of the
188 entire set of observed minerals, including cell parameter refinement of the major mineral phases.
189 The refined plagioclase unit-cell parameters follow a linear trend over the offset range (Fig. 3b).
190 The sample cell offset distance is the point of intersection between the offset trend line and the
191 literature least-squares trend line (Table 3). Once the offset calibration is applied to the
192 diffraction pattern, the refined plagioclase unit-cell parameters agree well with the expected
193 trend (Fig. 3c).

194 Refinement of XRD patterns with calculated sample cell offsets improves the accuracy not
195 only of plagioclase unit-cell parameters, but also of all other phases refined in CheMin samples.
196 For example, literature unit-cell parameters of Fe-Mg olivine (Table A1b; data table available in
197 csv format at github.com/shaunnamm/regression-and-minimization) vary consistently with one
198 another (Fig. 4a-f), just as in plagioclase, and can be used to calibrate cell offset for samples with
199 abundant olivine. Therefore, examining Mg-Fe olivine is an independent validation of the

This is a preprint, the final version is subject to change, of the American Mineralogist (MSA)
Cite as Authors (Year) Title. American Mineralogist, in press.
DOI: http://dx.doi.org/10.2138/am-2018-6124

calibration method. In CheMin samples with significant olivine and plagioclase, such as Rocknest, we observe the same internal inconsistency amongst olivine unit-cell parameters (Fig. 4a-f) as we do in those of plagioclase. In the Rocknest example, olivine compositions derived individually from each of the non-calibrated unit-cell parameters produced a range of $Mg_{1.03}Fe_{0.97}SiO_4$ to $Mg_{1.54}Fe_{0.46}SiO_4$ with a standard deviation of 0.20 Mg atoms per formula unit (apfu). Applying the plagioclase sample cell offset calibration method brought the olivine unit-cell parameters into internal consistency and into agreement with terrestrial trends (Fig. 4a-f). Additionally, the precision of olivine compositions produced by evaluation of individual unit-cell parameters versus composition was dramatically increased, with a range of $Mg_{1.15}Fe_{0.85}SiO_4$ to $Mg_{1.18}Fe_{0.82}SiO_4$ and a standard deviation of 0.01 Mg apfu.

The plagioclase sample cell offset calibration increases the accuracy of CheMin unit-cell parameters, and hence the derived major phase composition, beyond the original expectations (Blake et al. 2012). This new calibration is employed in the CheMin results of Morris et al. (2016), Rampe et al. (2017), Yen et al. (2017), Achilles et al. (2017), and in all subsequent publications.

CRYSTAL CHEMISTRY

Plagioclase and alkali feldspar

Feldspars are among the most common minerals in Earth's crust and that of other rocky bodies. The composition and ordering state of plagioclase and alkali feldspar provide important information regarding their igneous origins. Elemental substitution is common in K-feldspar (Treiman et al. 2016) and, to a lesser extent, in plagioclase. Minor chemical substitution can occur without resulting in significant deviation from observed pure K-Na or Na-Ca feldspar unit-

This is a preprint, the final version is subject to change, of the American Mineralogist (MSA)
Cite as Authors (Year) Title. American Mineralogist, in press.
DOI: http://dx.doi.org/10.2138/am-2018-6124

cell parameter trends (Morrison et al. 2017). In alkali feldspar, samples with up to 0.02 Ba or Cs apfu (Angel et al. 2013) and 0.008 Rb apfu (Dal Negro et al. 1978) exhibit unit-cell parameters corresponding to pure Na-K feldspar. Sanidine can incorporate up to 0.10 Fe^{3+} apfu without showing deviation from the Na-K trend (Kuehner and Joswiak 1996; Lebedeva et al. 1993; Morrison et al. 2017). Note that up to 0.09 Fe^{3+} apfu has been observed in K-feldspar found in martian meteorite samples (Hewins et al. 2017); if this amount were to occur in Gale crater samples, it would not be detectable in the CheMin XRD data. In plagioclase, up to 0.04 K apfu (Bambauer et al. 1967) and 0.02 Fe apfu (rruff.info) have been reported with no deviation from the pure Na-Ca plagioclase unit-cell parameter trends. Of all measured plagioclase/maskelynite compositions from martian meteorites, 97.6% contain less than 2 wt% minor oxides (e.g., Fe_2O_3, K_2O, MgO, MnO, TiO_2, BaO) (Papike et al. 2009; Santos et al. 2015; Wittmann et al. 2015; Nyquist et al. 2016; Hewins et al. 2017), abundances that are likely to be imperceptible in unit-cell parameter trends.

Plagioclase is the most abundant crystalline phase in every Gale crater sample analyzed with CheMin, except Windjana. CheMin plagioclase compositions estimated with the crystal-chemical method detailed in Morrison et al. (2017) are shown in Table 4. The analyzed plagioclase exhibits a broad compositional range [$An_{30(8)}$ to $An_{63(6)}$] with an average of $An_{40(11)}$. This range is compared with that of martian meteorites in Figure 5. The soil samples, Rocknest [$An_{49(4)}$] and Gobabeb [$An_{63(6)}$], exhibit notably higher Ca contents than the average plagioclase analyzed with CheMin. Plagioclase of the Murray Formation samples are very consistent with the Gale crater average and with one another [Murray average: $An_{38(2)}$]. The Stimson Formation samples show more variation [from $An_{30(8)}$ to $An_{52(5)}$], with little to no trend between the unaltered and altered samples.

This is a preprint, the final version is subject to change, of the American Mineralogist (MSA)
Cite as Authors (Year) Title. American Mineralogist, in press.
DOI: http://dx.doi.org/10.2138/am-2018-6124

Additionally, an alkali feldspar phase, sanidine, is observed in many of the CheMin samples in Gale crater (Fig. 6), with the highest abundance in Windjana [25.9(12) wt% of the crystalline material]. Estimated compositions and ordering of the alkali feldspars analyzed with the CheMin instrument in Gale crater are shown in Table 5. Alkali feldspars in Gale crater are completely disordered with compositions from $Or_{53(18)}$ to $Or_{87(5)}$ and an average of $Or_{74(17)}$. The composition and complete Al/Si disorder of sanidine points to a high-temperature, igneous formation with no prolonged thermal history (Gupta 2015; Treiman et al. 2016).

Pyroxene

To date, CheMin has observed three pyroxene phases in Gale crater: pigeonite, $(Mg,Fe,Ca)_2Si_2O_6$, with $P2_1/c$ symmetry; augite, $(Ca,Mg,Fe)_2Si_2O_6$, with $C2/c$ symmetry; and orthopyroxene, $(Mg,Fe,Ca)_2Si_2O_6$, with *Pbca* symmetry. The composition and structure of pyroxene crystallizing from basaltic magma is sensitive to the pressure and temperature in the magma. Therefore, characterizing pyroxene phases is critical to understanding magmatic history (Turnock et al. 1973; Lindsley 1983; Papike et al. 2009). Pyroxene is commonly zoned, which may be true of the pyroxene grains in Gale crater, but, given that CheMin samples bulk material and has a slightly lower resolution than a laboratory instrument, in addition to the lack of microscopy, we have not and likely cannot detect zonation in pyroxene grains. The pyroxene structure can incorporate significant amounts of non-quadrilateral components. High-Ca (Ca mole fraction > 0.5) pyroxene in martian meteorites, however, exhibits a relatively low amount of non-quadrilateral substitution (quadrilateral components: Mg, Fe, and Ca), with 99.8% of the 876 sample analyses reported in Papike et al. (2009), Santos et al. (2015), Wittmann et al. (2015), Nyquist et al. (2016), and Hewins et al. (2017) having less than 10% non-quadrilateral

This is a preprint, the final version is subject to change, of the American Mineralogist (MSA)
Cite as Authors (Year) Title. American Mineralogist, in press.
DOI: http://dx.doi.org/10.2138/am-2018-6124

cations. Elemental substitution occurs in low-Ca pyroxene, but to a lesser extent than in high-Ca pyroxene. Because of similarity in molar volume of the possible combinations of quadrilateral and non-quadrilateral components (Baker and Beckett 1999), it is impossible to determine a unique solution with X-ray diffraction data alone. Given the relatively low frequency of non-quadrilateral substitutions in martian meteorites, we limit our investigation to the Mg-Fe-Ca pyroxene system.

Empirical formulae for pigeonite in CheMin samples are given in Table 6 and compared with martian meteorites in Fig. 7. The pigeonite analyzed in Gale crater crosses a broad compositional range $\{[Mg_{0.95(12)-1.54(17)}Fe_{0.18(17)-1.03(9)}Ca_{0.00-0.28(6)}]_{\Sigma=2}Si_2O_6\}$ with an average of $Mg_{1.18(19)}Fe_{0.72(7)}Ca_{0.10(9)}Si_2O_6$. Samples of the Murray formation (Confidence Hills, Mojave2, and Telegraph Peak) and the Stimson formation (Big Sky, Lubango, and Okoruso) have significantly smaller compositional ranges {Murray: $[Mg_{1.05(23)-1.10(20)}Fe_{0.83(17)-0.94(10)}Ca_{0.00-0.07(10)}]_{\Sigma=2}Si_2O_6$; Stimson: $[Mg_{1.39(7)-1.54(17)}Fe_{0.18(17)-0.48(10)}Ca_{0.13(5)-0.28(6)}]_{\Sigma=2}Si_2O_6\}$ than rock samples collected from the Gale crater plains and soil targets. Stimson pigeonite has notably high Mg and Ca content (and, therefore, low Fe) relative to the rest of the Gale samples, with the altered sample, Lubango, having the highest Mg and Ca contents of all samples measured.

Augite was detected in abundance significant enough for refinement in only three Gale crater samples: Rocknest and Gobabeb (soils) and the Windjana sandstone. Augite composition is given in Table 7 and compared with martian meteorites in Fig. 7. Augites analyzed with CheMin in Gale crater fall in a narrow compositional range $\{[Mg_{0.89(8)-1.03(7)}Ca_{0.72(4)-0.75(4)}Fe_{0.21(9)-0.38(9)}]_{\Sigma=2}Si_2O_6\}$, with an average of $Mg_{0.96(6)}Ca_{0.73(2)}Fe_{0.31(8)}Si_2O_6$.

The chemical composition of orthopyroxene analyzed with CheMin in Gale crater is given in Table 8 and compared with martian meteorites in Fig. 7. Orthopyroxene has a narrow range of

This is a preprint, the final version is subject to change, of the American Mineralogist (MSA)
Cite as Authors (Year) Title. American Mineralogist, in press.
DOI: http://dx.doi.org/10.2138/am-2018-6124

292 $[Mg_{0.69(7)-0.86(20)}Fe_{1.14(20)-1.31(7)}Ca_{0.00-0.04(4)}]_{\Sigma=2}Si_2O_6$, with an average of
293 $Mg_{0.79(6)}Fe_{1.20(6)}Ca_{0.01(2)}Si_2O_6$.
294
295 **Olivine**
296 Mg-rich olivine, with < 20 wt% Fe substituting for Mg, is the dominant mineral phase in
297 many ultramafic rocks on Earth. It is one of the first phases to crystallize in basaltic and
298 ultramafic melts and, as a result, it can preserve important information about the bulk rock's
299 temperature and pressure history (Papike et al. 2009; Lee et al. 2009; Filiberto and Dasgupta
300 2015). On Earth, the olivine structure can accommodate significant amounts of Ca (up to 0.19
301 apfu) and/or Mn (up to 1 apfu) while still adhering to the Fe-Mg olivine trends in unit-cell
302 parameters (Fig. 4a-f). The olivine composition in martian meteorites reported by McSween and
303 Treiman (1998), Papike et al. (2009), and Hewins et al. (2017), have less than 0.027 Ca apfu,
304 and/or 0.038 Mn apfu (rarely with trace Ti, Cr, Ni, and/or Co). Therefore, it is likely that we can
305 limit the range of non-Fe-Mg components in olivine analyzed with CheMin to that reported for
306 martian meteorites.
307 In contrast to martian meteorites, which commonly contain olivine, only 3 of the 13 samples
308 analyzed with CheMin contain detectable amounts of olivine. It is possible that these other 10
309 samples never contained olivine; however, it is more likely that they have experienced more
310 extensive aqueous alteration during their formation or diagenesis and, given that olivine is most
311 susceptible of the silicates to aqueous alteration, it was altered to another phase or dissolved
312 entirely. In either scenario, this finding emphasizes the importance of recognizing that Gale
313 crater materials are substantially different from martian meteorites, likely because of the effects
314 of secondary weathering and alteration.

This is a preprint, the final version is subject to change, of the American Mineralogist (MSA)
Cite as Authors (Year) Title. American Mineralogist, in press.
DOI: http://dx.doi.org/10.2138/am-2018-6124

315 The compositions of olivine analyzed by CheMin are listed in Table 9. The average olivine
316 composition is $Mg_{1.19(12)}Fe_{0.81(12)}SiO_4$ with a range of 1.08(3) to 1.45(7) Mg apfu. The average
317 olivine composition of the samples analyzed in Gale crater is very similar to the average olivine
318 composition of martian meteorites ($Mg_{1.21}Fe_{0.76}Mn_{0.02}Ca_{0.01}SiO_4$) (Papike et al. 2009; Hewins et
319 al. 2017) and the range is well within that of martian meteorites (Fig. 8). The Windjana
320 sandstone has a noticeably more magnesian composition [$Mg_{1.35(7)}Fe_{0.65(7)}SiO_4$] than that of the
321 wind-blown soils [soil average = $Mg_{1.11(4)}Fe_{0.89(4)}SiO_4$]. Compositions of the wind-blown
322 sediment samples, Rocknest and Gobabeb, are considered to be representative of the martian soil
323 and to have average crustal composition, representing a global mixture of martian dust and
324 locally or regionally derived wind-blown soil (Bish et al. 2013; Blake et al. 2013; Achilles et al.
325 2017). The similarity in composition of Rocknest [$Fo_{57(2)}$] and Gobabeb [$Fo_{54(2)}$] echoes the
326 assertion that these unconsolidated sediments may represent average crustal composition.
327
328 **Magnetite**
329 The cubic spinel structure can accommodate Fe, Mg, Al, Ti, and a variety of transition metals
330 and other elements, making it impossible to determine the composition of a spinel based on the
331 single parameter than can be determined with CheMin - the *a* cell dimension (Morrison et al.
332 2017). We detected a spinel phase in each of the Gale crater samples analyzed with CheMin. It is
333 important to note that the Gale samples are rocks or loose sediment and therefore may contain
334 spinel crystals of varying compositions; given that we cannot isolate single grains with powder
335 X-ray diffraction, the spinel peaks, and resulting unit-cell parameters, represent an average of all
336 spinel grains in an analyzed sample. Magnetite ($Fe^{2+}Fe^{3+}{}_2O_4$) or Ti-magnetite [as well as minor
337 amount of chromite ($Fe^{2+}Cr_2O_4$)] is present in martian meteorites and was detected on the
338 martian surface by the MER Mössbauer spectrometers, particularly at Gusev crater (Morris et al.

This is a preprint, the final version is subject to change, of the American Mineralogist (MSA)
Cite as Authors (Year) Title. American Mineralogist, in press.
DOI: http://dx.doi.org/10.2138/am-2018-6124

2006, 2008). Martian meteorites contain a significant proportion of chromite, $Fe^{2+}Cr_2O_4$, (~18% of all samples cited in Morrison et al. 2017), and much of the magnetite contains significant proportions of Al (up to 1.01 apfu, assuming no site vacancy), Ti (up to 0.95 apfu), and Mg (up to 0.43 apfu), with minor (<0.05 apfu) Si, V, Mn, Ca, Na, Ni, Co, and Zn (Morrison et al. 2017).

Given the large compositional range accommodated by the spinel structure and frequent occurrence of minor elements in martian meteorite magnetite, we explored the possible range of composition in magnetite detected in Gale crater. In Figure 9, the literature trends of Fe versus the *a* unit-cell parameter are given for (Fe,□), (Fe,Al), (Fe,Ti), (Fe,Mg), (Fe,Cr), (Fe,Ni), (Fe,Zn), (Fe,V) (Fe,Al,□), (Fe,Mg,Al), (Fe,Mn,Ti), (Fe,Mg,Cr), and (Fe,Mg,Ti) spinel oxide phases. The complexity of Figure 9, a result of variation in cation size, site occupancies, and oxidation state of multi-element composition, illustrates that numerous chemical combinations can produce a given *a* cell edge in the spinel structure.

Based on the unit-cell dimensions refined with CheMin, in combination with meteorite and mission data, we assume that most of the spinels analyzed with CheMin in Gale crater can be ascribed to a solid solution between pure magnetite (Fe) and cation-deficient magnetite (Fe,□), which gives an average composition of $Fe_{2.83(5)}\square_{0.14}O_4$ and a range of 2.75(5) to 2.90(5) Fe per formula unit. However, other reasonable substitutions for Fe could produce the unit-cell parameter of the Gale crater spinels, such as Al, Mg, and Cr, each of which have implications on the environment of formation. As detailed in Treiman et al. (2016), chromite or chromian magnetite is a common accessory phase in basalt, while cation-deficient magnetite is often associated with the diagenetic oxidation of olivine, and significant amounts of Mg in magnetite are associated with rare geologic settings (impact spherules, meteorite fusion crusts, rare carbonatites) that are unlikely in general for the Gale crater materials. Ti is a common substituent

This is a preprint, the final version is subject to change, of the American Mineralogist (MSA)
Cite as Authors (Year) Title. American Mineralogist, in press.
DOI: http://dx.doi.org/10.2138/am-2018-6124

362 in magnetite formed on Earth and found in martian meteorites, but the Gale crater refined unit-
363 cell dimensions are too small for a significant (>0.08 apfu) Ti substitution (Fig. 9). Chromite or
364 heavily Cr-enriched magnetite fits the geologic setting of Gale crater, but elevated amounts are
365 not detected in bulk sample analysis, making such a composition unlikely (Treiman et al. 2017).
366 Therefore, it is most likely that the spinel phases observed in Gale are mixtures of magnetite to
367 cation-deficient magnetite, possibly with minor amounts of Al, Mg, Cr, and/or chromite.

368 Proposed magnetite compositions of Gale crater samples analyzed with CheMin are given in
369 Table 10. The unit-cell dimension, and resulting estimated compositions, are relatively similar
370 across the Gale crater samples, with the exception of the Murray formation samples, which have
371 notably smaller unit-cell dimensions and, therefore, if we assume a magnetite to cation-deficient
372 magnetite composition, are distinctly more cation deficient (average: $Fe_{2.77(2)}\square_{0.23}O_4$) than the
373 Gale crater average and even more so than the Stimson formation samples (Average:
374 $Fe_{2.88(2)}\square_{0.12}O_4$).

375

376 **Alunite-Jarosite**

377 The discovery of alunite-jarosite group minerals on Mars has important implications for
378 ancient martian weathering environments (Klingelhöfer et al. 2004; Zolotov and Shock 2005;
379 Morris et al. 2006; Golden et al. 2008; Swayze et al. 2008; Mills et al. 2013; Hurowitz et al.
380 2017). Alunite-jarosite group minerals include alunite, $KAl_3(SO_4)_2(OH)_6$; jarosite,
381 $KFe^{3+}_3(SO_4)_2(OH)_6$; natroalunite, $NaAl_3(SO_4)_2(OH)_6$; natrojarosite, $NaFe^{3+}_3(SO_4)_2(OH)_6$;
382 ammonioalunite, $NH_4Al_3(SO_4)_2(OH)_6$; ammoniojarosite, $NH_4Fe^{3+}_3(SO_4)_2(OH)_6$; and
383 hydroniumjarosite, $(H_3O)Fe^{3+}_3(SO_4)_2(OH)_6$. Figure 10 shows the cell parameters of the 'jarosite'
384 detected in the Mojave2 sample plotted on the alunite-jarosite quadrilateral (Morrison et al.
385 2017). The refined unit-cell parameters correspond to a jarosite composition of

This is a preprint, the final version is subject to change, of the American Mineralogist (MSA)
Cite as Authors (Year) Title. American Mineralogist, in press.
DOI: http://dx.doi.org/10.2138/am-2018-6124

386 $(K_{0.51(12)}Na_{0.49})(Fe_{2.68(7)}Al_{0.32})(SO_4)_2(OH)_6$. The uncertainties reported here for the jarosite
387 compositions are inaccurately low because the equations used to calculate the alunite-jarosite
388 compositions only incorporate uncertainty from the unit-cell parameters and not the uncertainty
389 of the natural mineral system.
390

391 ## PETROLOGIC INTERPRETATIONS: MAFIC MINERALS

392 Determining the mineral chemistry of mafic minerals has direct implications for the
393 interpretation of soils and rocks in Gale crater. As an example of the petrologic value of these
394 determinations, we consider the species and composition of the pyroxene and olivine phases
395 observed in Gale crater. Fig. 11a-c show the compositional ranges for pyroxene and olivine, as
396 given in Tables 6 to 9, plotted on a conventional pyroxene quadrilateral diagram. Also shown are
397 the low-pressure ($P < 2$ kbar) temperature contours and three-phase triangles (orthopyroxene +
398 pigeonite + augite) in 100°C intervals from Lindsley (1983). Note that for a pyroxene to be
399 correctly plotted with respect to the isotherms requires that the effects of non-quadrilateral
400 components in the pyroxene be accounted for via the projection scheme reported in Lindsley
401 (1983). Although this is not a correction we can make (since, as discussed above and in Morrison
402 et al., 2017a, the proportions of non-quadrilateral components in the pyroxenes analyzed with
403 CheMin in Gale crater cannot be calculated from their unit cell parameters), by analogy with the
404 compositions of pyroxenes in martian meteorites, we assume that pyroxenes observed in Gale
405 crater also have relatively minor abundances of non-quadrilateral constituents and, thus, the
406 temperature error associated with their un-corrected placement on the quadrilateral is likely to be
407 low. Olivine compositions are plotted below the enstatite-ferrosilite join at the appropriate
408 Fe/Mg ratios. For olivines with Mg/(Mg+Fe) like those in Gale crater (~0.54-0.68, Fig. 8),

This is a preprint, the final version is subject to change, of the American Mineralogist (MSA)
Cite as Authors (Year) Title. American Mineralogist, in press.
DOI: http://dx.doi.org/10.2138/am-2018-6124

409 equilibrium orthopyroxenes have similar Fe/Mg ratios and, in this compositional range, the
410 olivine-orthopyroxene Fe-Mg exchange coefficient is nearly independent of temperature (Sack,
411 1980). Figures 11a-c include all of the applicable samples analyzed with CheMin, and support
412 several significant petrologic inferences, including: (1) comparisons and possible consanguinity
413 of materials, (2) evidence for single or multiple sediment sources, (3) changes in sediment
414 provenance, and (4) effects of chemical alteration.

415 (1) Pyroxene and olivine compositions can provide crucial clues to the consanguinity of
416 samples. Consider the mafic minerals of the two analyzed sands, Rocknest and Gobabeb (Fig.
417 11a). Rocknest is a sand shadow analyzed very early in the mission (Blake et al. 2013); Gobabeb
418 is a sample of the active Namib sand dune, part of the Bagnold Dune Field, ~10 km distant from
419 Rocknest (Achilles et al. 2017). Fig. 11a shows that the pyroxenes and olivine observed in
420 Rocknest and Gobabeb have identical compositions within uncertainties, which suggests that
421 both represent the same sand mass, however, the distinctly different plagioclase compositions
422 ($An_{49(4)}$ and $An_{63(6)}$ in Rocknest and Gobabeb, respectively) suggest the possibility of different
423 parentage over time (Achilles et al. 2017). Similarly, the adjacent samples John Klein and
424 Cumberland (Fig. 11b), both drilled in the Yellowknife Bay area, have pyroxenes with identical
425 compositions (within uncertainty). This result is expected but still encouraging, as these two drill
426 samples were within meters of each other in the same stratigraphic horizon. In another example,
427 the drill samples Confidence Hills, Mojave2, and Telegraph Peak (Fig. 11c) were taken within a
428 few meters of stratigraphy in a single section of the Murray mudstone formation (Rampe et al.
429 2017). The pigeonites in those samples (the only mafic mineral present) have identical
430 composition within uncertainty, consistent with their common stratigraphic positions.

This is a preprint, the final version is subject to change, of the American Mineralogist (MSA)
Cite as Authors (Year) Title. American Mineralogist, in press.
DOI: http://dx.doi.org/10.2138/am-2018-6124

(2) Chemical equilibria (or lack thereof) among the mafic minerals can suggest whether a sediment had a single basalt source or multiple sources. Mafic minerals (olivine, low-Ca pyroxene, and high-Ca pyroxene) in the sand samples Rocknest and Gobabeb have widely differing Fe/Mg ratios, and thus are consistent with several basaltic sources (Fig. 11a), as might be reasonable for a regional sand sheet such as the current Bagnold Dunes. However, this interpretation is not certain, as this range of mineral compositions could have formed in a single igneous rock as it evolved during crystallization – the magnesian augite forming first, and the less magnesian pigeonite forming later, at lower temperatures. A similar pattern, though not identical, is seen in the nakhlite martian meteorites (Treiman 2005). In those basaltic rocks, augite and olivine were the early-crystallizing mafic silicates, and were followed much later by pigeonite and orthopyroxene, both significantly more ferroan than the augite. A similar trend in pyroxene and olivine is observed in the Windjana drill sample, Fig. 11b. The chemical compositions of the rocks near Windjana (the Kimberley area) imply several sediment sources (Treiman et al. 2016; Le Deit et al. 2016; Treiman and Medard 2016; Siebach et al. 2017).

(3) Mafic minerals can be strong indicators of changing sediment sources (i.e., provenance). Take, for example, the contrast between the mineralogy of the Murray mudstone samples (Confidence Hills, Mojave2, and Telegraph Peak; Rampe et al. 2017) and the mineralogy of the overlying Stimson sandstone (Big Sky, Greenhorn, Lubango and Okoruso; Yen et al. 2017). The mafic mineralogy of those two sample groups is quite different (Fig. 11c): the Murray mudstones (in shades of purple) having only pigeonite of very low Ca content and intermediate Fe/Mg ratio, while the Stimson sandstone (shades of blue and green) contains magnesian, relatively high-Ca pigeonite and very ferroan orthopyroxene (approaching ferrosilite composition). Clearly, these sediments are not closely related, and stratigraphic studies along Curiosity's traverse have

This is a preprint, the final version is subject to change, of the American Mineralogist (MSA)
Cite as Authors (Year) Title. American Mineralogist, in press.
DOI: http://dx.doi.org/10.2138/am-2018-6124

454 demonstrated the presence of an unconformity, with significant topographic relief, between the
455 Murray and Stimson (Watkins et al. 2017).
456 (4) The mafic mineralogy of a sediment can record evidence about the chemical processes of its
457 diagenesis and alteration. There is extensive evidence of widespread, though volumetrically
458 minor, chemical alteration and diagenesis of sediments in Gale crater, including formation of
459 smectitic clay from olivine (Vaniman et al. 2014; Bristow et al. 2015), acid-sulfate alteration to
460 produce jarosite-group minerals among others (Rampe et al. 2017), and silicification surrounding
461 fractures (Yen et al. 2017). Any of these alteration processes could affect the mafic silicate
462 minerals of the sediments. John Klein and Cumberland have been sufficiently weathered such
463 that all or most of the olivine that was likely present in the source material has altered to a
464 smectitic clay (Vaniman et al. 2014). The Murray mudstones of Pahrump Hills (Rampe et al.
465 2017) have been altered by varying degrees of acid-sulfate solutions, also resulting in the
466 complete loss of any original olivine. The silicified Stimson sandstones, Greenhorn and
467 Lubango, have orthopyroxene compositions similar to those of their unsilicified counterparts,
468 Big Sky and Okoruso. The abundance of pigeonite in altered Stimson samples is much
469 diminished (5 to 6 wt% of the crystalline material) compared to the unaltered samples (21 wt%
470 crystalline), and the composition of the remaining pigeonite (especially in Lubango) is
471 noticeably more magnesian than that of the unaltered samples nearby (Fig. 11c). However, note
472 that pigeonite is so near the detection limit in the altered Stimson samples that the unit-cell
473 parameters of Greenhorn could not be accurately refined and the uncertainty of the unit-cell
474 parameters and resulting estimated composition of Lubango is high. Therefore, it is difficult to
475 make an accurate comparison of unaltered versus altered Stimson pigeonite composition.
476

This is a preprint, the final version is subject to change, of the American Mineralogist (MSA)
Cite as Authors (Year) Title. American Mineralogist, in press.
DOI: http://dx.doi.org/10.2138/am-2018-6124

BULK COMPOSITION OF AMORPHOUS MATERIALS

All martian rocks and soils examined with CheMin contain significant amounts of X-ray amorphous material, ranging from 20 to 64 wt%. The amorphous and clay mineral components of Gale crater samples are measured and modeled using the full pattern fitting program FULLPAT (Chipera and Bish 2002, 2013). Sample patterns and reference intensity ratios (RIRs) from a suite of natural and synthetic amorphous and clay mineral samples are measured in a CheMin-equivalent CheMin IV instrument at NASA Johnson Space Center. The amorphous component(s) in the Mars samples are identified and modeled by fitting these known and measured library patterns to the Mars data. The characterization of amorphous materials using X-ray diffraction alone is problematic because such materials lack the translational periodicity needed to produce sharp diffraction peaks. However, limits on the bulk amorphous material composition and proportion in a given sample can be estimated by comparing its bulk elemental composition from the APXS (Campbell et al. 2012; Gellert et al. 2015; Thompson et al. 2016; O'Connell-Cooper 2017) with that of its crystalline component from CheMin (see below). For each sample, the APXS instrument measures the < 150 μm post-sieved material dumped onto the martian surface by SA/SPaH after analyses with CheMin are complete. This is the same reservoir of material from which CheMin obtains its sample.

We estimated the chemical composition of amorphous material at the lower limit of its proportion with the following matrix equation (Equation 1):

$$\mathbf{A} = \mathbf{B} - \alpha\mathbf{C}, \quad (1)$$

where **A** is the X-ray amorphous component composition; **B** is the bulk sample composition measured by APXS; α is a scalar that corresponds to the maximum possible fraction of

This is a preprint, the final version is subject to change, of the American Mineralogist (MSA)
Cite as Authors (Year) Title. American Mineralogist, in press.
DOI: http://dx.doi.org/10.2138/am-2018-6124

crystalline material in a sample constrained by mass-balance; and **C** is the bulk crystalline composition (Table 11).

We calculate bulk crystalline composition by summing the crystal-chemically derived major phase compositions and the ideal chemical compositions of the minor crystalline phases, with each phase scaled in proportion to its estimated abundance, determined by Rietveld refinement (Table 11-12a-e). Alpha (Table 12a-e) is calculated by scaling and subtracting the crystalline composition from the APXS-measured bulk composition until an element in the bulk composition is driven to zero. The limiting element in the soil samples is Mg and the limiting element of the Yellowknife Bay formation, Buckskin, and the altered Stimson formation samples is Al; however, the remaining Gale samples are limited by either Ca or K, with no apparent trend amongst the samples or formations.

In contrast to α, which is derived from chemical composition, the amorphous-component proportion estimated by FULLPAT is derived solely from the diffracted intensities of the crystalline and amorphous materials in the XRD pattern. Fig. 12 compares the minimum proportion of amorphous material (i.e., 1- α) versus the FULLPAT estimated amorphous-component proportion for each of the CheMin samples (Blake et al. 2013; Treiman et al. 2014, 2016; Vaniman et al. 2014; Morris et al. 2016; Achilles et al. 2017; Rampe et al. 2017; Yen et al. 2017). The method presented herein produces an estimate of the maximum proportion of crystalline material and, consequently, the minimum amount of amorphous material (Table 12a-e). It is critical to point out that this method does not account for minor or trace elements that are not solved for in our crystal-chemical estimation of major phase composition (Morrison et al. 2017) nor does it account for departure from the ideal composition of minor phases. The

This is a preprint, the final version is subject to change, of the American Mineralogist (MSA)
Cite as Authors (Year) Title. American Mineralogist, in press.
DOI: http://dx.doi.org/10.2138/am-2018-6124

elements Mn, Cr, Al, and Ti are of particular concern because they are commonly minor components in pyroxene, olivine, and/or magnetite (see previous section).

X-ray amorphous materials may contain crystalline phases present at quantities below the detection limit of CheMin (<1 to 3 wt%) and/or materials that do not coherently diffract X-rays (e.g., amorphous or short-range ordered materials). The composition and proportion of amorphous material in a sample provide important information regarding the nature of the source material and post-depositional processes. These materials may contain many components, including allophane/hisingerite, mafic glass, felsic glass, Opal-A and Opal CT, short-range ordered (SRO) sulfates, and nanophase iron oxides (Morris et al. 2006, 2008, 2016; Bish et al. 2013; Blake et al. 2013; Rampe et al. 2014; Achilles et al. 2016, Yen et al. 2017). Therefore, characterizing the amorphous material is an important part of assessing the nature of ancient environments in Gale crater. Below, we provide several examples of the amorphous component compositions and their geologic implications.

The active dune material (Gobabeb) contains a high proportion of amorphous material (lower limit = ~42 wt%) with SiO_2, FeO, Al_2O_3 and SO_3 as its major constituent oxides (Table 12a). Possible phases responsible for this chemistry could include maskelynite, amorphous silica, nanophase iron oxides, and sulfates (Achilles et al. 2017). These phases suggest a history of impact, oxidation, aqueous, and likely physical (e.g., eolian) processes involved in the formation of the amorphous materials. The inactive, armored dune (Rocknest) has a lower amount of amorphous material (lower limit = ~20 wt%) and a significantly lower proportion of SiO_2 and Al_2O_3, but a much greater SO_3. The increased amount of SO_3 is attributed to the accumulation of wind-blown dust because of the inactivity of the Rocknest dune (Achilles et al. 2017). The disparity in SiO_2 content between the two soil samples is poorly understood, but we have

This is a preprint, the final version is subject to change, of the American Mineralogist (MSA)
Cite as Authors (Year) Title. American Mineralogist, in press.
DOI: http://dx.doi.org/10.2138/am-2018-6124

545 observed that high SiO_2 proportions trends with high amorphous content in Gale crater samples;
546 additionally, Achilles et al. (2017) proposes that the amorphous silica material in Gobabeb could
547 be derived from the nearby Murray and altered Stimson strata. CheMin did not detect minerals
548 containing P, Cl, Cr, Mn and Ti; therefore, these elements are assumed to be incorporated with
549 the X-ray amorphous component, but, as discussed previously, trace or minor amounts of these
550 elements could be included in crystalline phases. Chlorine may be in the form of various salts of
551 chlorides, perchlorates, and/or chlorates, but if present, these salts occur in quantities well below
552 the detection limit of CheMin. Oxychlorine compounds (e.g., perchlorates and possibly
553 chlorates) have been detected by the MSL Sam Analysis at Mars (SAM) instrument (Sutter et al.
554 2017). Chromium, Mn, and Ti may be present in trace quantities in primary igneous phases (as
555 discussed above) or as oxides and with other secondary alteration phases that are below the
556 detection limit of CheMin. Likewise, no P-containing minerals were detected with CheMin, but
557 may be present at quantities below the detection limit. Phosphorus may also be present in
558 secondary alteration phases or chemisorbed on nanophase weathering products (e.g., Rampe et
559 al. 2016).

560 The amorphous component of the Murray formation is somewhat similar to that of the
561 scooped soils or the altered Stimson formation, with few noteworthy trends. An obvious
562 exception is the Buckskin mudstone, which is composed predominately of SiO_2 (lower limit =
563 ~76 wt%) along with SO_3 (~7.6 wt%), FeO_T (total Fe content calculated as FeO; ~4.8 wt%),
564 TiO_2 (~2.8 wt%), and P_2O_5 (~2.2 wt%) as the most abundant oxides (Table 12c). Other elements
565 (e.g., Cl) are also present as minor or trace quantities in the amorphous component (Table 12c).
566 Possible candidate phases in the amorphous material are opal-A or high-Si glass, volatile-bearing
567 mixed-cation sulfates, phosphates, and chlorides/perchlorates/chlorates, and Ti- and Fe-oxides

This is a preprint, the final version is subject to change, of the American Mineralogist (MSA)
Cite as Authors (Year) Title. American Mineralogist, in press.
DOI: http://dx.doi.org/10.2138/am-2018-6124

(Morris et al. 2016). Opaline silica could have formed during diagenesis of high-SiO_2 glass or as a residue of acidic leaching of the sediments or source sediments (Morris et al. 2016). The other secondary phases may have been derived during diagenesis from multiple episodes of aqueous alteration with varying solution compositions and temperatures.

The significantly greater average abundance of amorphous material in Greenhorn and Lubango samples (lower limits = ~64-71 wt%) versus that of the Big Sky and Okoruso samples (lower limits = ~14-43 wt%) (Table 12e), supports the assertion that the former two Stimson samples have been altered while the latter are significantly less-so (or "unaltered") (Yen et al. 2017). As observed in the general trend of all Gale crater samples, the Stimson samples show that Si content, both in absolute abundance and normalized to amorphous-component abundance, increases with increasing amorphous-component proportion. The opposite trend is observed in Fe content. In the Stimson, these trends can likely be attributed to the partial dissolution of pyroxene, with plagioclase less affected by the alteration undergone by Greenhorn and Lubango. Magnetite abundance remains relatively constant throughout the Stimson samples, having been less affected by alteration or, alternatively, having been precipitated as a secondary phase during alteration (Yen et al. 2017). The ratios of plagioclase to magnetite remain relatively consistent across the Stimson, but the ratio of plagioclase to pyroxene is ~1.4 in unaltered Stimson and ~3.0 in altered Stimson samples, showing preferential dissolution of pyroxene. Note that small amounts of an alkali feldspar phase and fluorapatite were detected in Big Sky and Okoruso, but not in the altered Stimson samples; this absence could indicate that these phases were dissolved during alteration or they could simply be below the detection limit of the instrument. Unfortunately, the crystalline abundances of the alkali feldspar and fluorapatite are too low to

This is a preprint, the final version is subject to change, of the American Mineralogist (MSA)
Cite as Authors (Year) Title. American Mineralogist, in press.
DOI: http://dx.doi.org/10.2138/am-2018-6124

590 make any meaningful comparison between the P and K contents of the crystalline and
591 amorphous materials.

592 Detailed discussion of the implications of amorphous material composition on the geologic
593 setting and processes for Rocknest, John Klein/Cumberland, Windjana, Confidence
594 Hills/Mojave2/Telegraph Peak, Buckskin, Big Sky/Greenhorn/Lubango/Okoruso, and Gobabeb
595 can be found in Blake et al. (2013), Vaniman et al. (2014), Treiman et al. (2016), Rampe et al.
596 (2017), Morris et al. (2016), Yen et al. (2017), and Achilles et al. (2017), respectively.
597

598 ## IMPLICATIONS

599 Crystal-chemical algorithms were applied to the martian rock and sediment samples analyzed
600 by the CheMin X-ray diffraction instrument onboard the MSL Curiosity rover in Gale crater. We
601 report newly refined mineral chemistries for loose, unconsolidated soil comprising global
602 martian dust and regional sediments (Achilles et al. 2017), as well as drilled samples of
603 sedimentary rock from the Yellowknife Bay, Kimberley, Murray (Morris et al. 2016; Rampe et
604 al. 2017), and Stimson (Yen et al. 2017) formations. These measurements constitute the first
605 definitive and quantitative mineralogical analyses of the martian surface. In combination with
606 data from Curiosity's other instruments, they are revolutionizing our understanding of martian
607 mineralogy, geochemistry, and the nature of habitable environments on early Mars.
608

609 ## ACKNOWLEDGEMENTS

610 We would like to acknowledge the support of the JPL engineering and Mars Science Laboratory (MSL)
611 operations team. The study benefited from discussions with Mike Baker regarding martian meteorite
612 compositions. We would like to thank Michael A. Velbel, an anonymous reviewer, and Bradley Jolliff for

their helpful reviews of this manuscript. This research was supported by NASA NNX11AP82A, MSL Investigations, and by the National Science Foundation Graduate Research Fellowship under Grant No. DGE-1143953. Any opinions, findings, or recommendations expressed herein are those of the authors and do not necessarily reflect the views of the National Aeronautics and Space Administration or the National Science Foundation.

REFERENCES CITED

Achilles, C.N., Downs, R.T., Ming, D.W., Rampe, E.B., Morris, R.V., Treiman, A.H., Morrison, S.M., Yen, A.S., Vaniman, D.T., Blake, D.F., Bristow, T.F., Chipera, S.J., Ewing, R.C., Ehlmann, B.L., Crisp, J.A., Gellert, R., Fendrich, K.V., Craig, P.I., Grotzinger, J.P., Des Marais, D.J., Farmer, J.D. Sarrazin, P.C., and Morookian, J.M. (2017) Mineralogy of an active eolian sediment from the Namib dune, Gale crater, Mars. Journal of Geophysical Research: Planets, Bagnold Dunes Special Issue (in press).

Allison, M. (1997) Accurate analytic representations of solar time and seasons on Mars with applications to the Pathfinder/Surveyor missions. Geophysical Research Letters, 24, 1967-1970.

Anderson R.C., Jandura, L., Okon, A.B., Sunshine, D., Roumeliotis, C. Beegle, L.W., Horowitz, J., Kennedy, B., Limonadi, D., McCloskey, S., Robinson, M. Seybold, C., and Brown, K. (2012) Collecting Samples in Gale crater, mars; an overview of the Mars Science Laboratory Sample Acquisition, Sample Processing and Handling System.Space Science Reviews, 170:57-75.

Angel, R.J., Ross, N.L., Zhao, J., Sochalski-Kolbus, L., Krüger, H., and Schmidt, B.C. (2013) Structural controls on the anisotropy of tetrahedral frameworks: the example of monoclinic feldspars. European Journal of Mineralogy, 25(4), 597-614.

Baker, M.B., and Beckett, J.R. (1999) The origin of abyssal peridotites: a reinterpretation of constraints based on primary bulk compositions. Earth and Planetary Science Letters, 171(1), 49-61.

Bambauer, H.U., Corlett, M., Eberhard, E., and Viswanathan, K. (1967) Diagrams for the determination of plagioclases using X-ray powder methods (Part III of laboratory investigations of plagioclases). Schweizerische Mineralogische und Petrographische Mitteilungen, 47, 333-349.

Bish, D.L., Blake, D.F., Vaniman, D.T., Chipera, S.J., Morris, R.V., Ming, D.W., Treiman, A.H., Sarrazin, P., Morrison, S.M., Downs, R.T., Achilles, C.N., Yen, A.S., Bristow, T.F., Crisp, J.A., Morookian, J.M., Farmer, J.D., Rampe, E.B., Stolper, E.M., Spanovich, N., and MSL Science Team (2013) X-ray diffraction results from Mars Science Laboratory: mineralogy of Rocknest at Gale crater. Science, 27, 341, 1238932.

Blake, D., Vaniman, D., Achilles, C., Anderson, R., Bish, D., Bristow, T., Chen, C., Chipera, S., Crisp, J., Des Marais, D., Downs, R.T., Farmer, J., Feldman, S., Fonda, M., Gailhanou, M., Ma, H., Ming, D.W., Morris, R.V., Sarrazin, P., Stolper, E.M., Treiman, A., and Yen, A. (2012) Characterization and calibration of the CheMin mineralogical instrument on Mars Science Laboratory. Space Science Reviews, 170, 341-399.

Blake, D.F., Morris, R.V., Kocurek, G., Morrison, S.M., Downs, R.T., Bish, D.L., Ming, D.W., Edgett, K.S., Rubin, D., Goetz, W., Madsen, M.B., Sullivan, R., Gellert, R., Campbell, I., Treiman, A.H., McLennan, S.M., Yen, A.S., Grotzinger, J., Vaniman, D.T., Chipera, S.J., Achilles, C.N., Rampe, E.B., Sumner, D., Meslin, P-Y., Maurice, S., Forni, O., Gasnault, O., Fisk, M., Schmidt, M., Mahaffy, P., Leshin, L.A., Glavin, D., Steele, A., Freissinet, C., Navarro-González, R., Yingst, R.A., Kah, L.C., Bridges, N., Lewis, K.W., Bristow, T.F., Farmer, J.D., Crisp, J.A., Stolper, E.M., Des Marais, D.J.,

Sarrazin, P., and MSL Science Team (2013) Curiosity at Gale crater, Mars: characterization and analysis of the Rocknest sand shadow. Science, 341, 1239505.

Bristow, T.F., Bish, D.L., Vaniman, D.T., Morris, R.V., Blake, D.F., Grotzinger, J.P., Rampe, E.B., Crisp, J.A., Achilles, C.N., Ming, D.W., Morris, R.V., Bristow, T.F., Morrison, S.M., Baker, M.B., Rampe, E.B., Downs, R.T., Filiberto, J., Glazner, A.F., Gellert, R., Thompson, L.M., Schmidt, M.E., Le Deit, L., Wiens, R.C., McAdam, A.C., Achilles, C.N., Edgett, K.S., Farmer, J.D., Fendrich, K.V., Grotzinger, J.P., Gupta, S., Morookian, J.M., Newcombe, M.E., Rice, M.S., Spray, J.G., Stolper, E.M., Sumner, D.Y., Vasavada, A.R., and Yen, A.S. (2015) The origin and implications of clay minerals from Yellowknife Bay, Gale crater, Mars. American Mineralogist, 100, 824-836.

Campbell, J.L., Perrett, G.M., Gellert, R., Andrushenko, S.M., Boyd, N.I., Maxwell, J.A., King, P.l, and Schofield, Celest D.M. (2012) Calibration of the Mars Science Laboratory Alpha Particle X-ray Spectrometer.Space Science Reviews, 170:319-340.

Chipera, S.J., and Bish, D.L. (2002) FULLPAT: A full-pattern quantitative analysis program for X-ray powder diffraction using measured and calculated patterns. Journal of Applied Crystallography, 35, 744-749.

Chipera, S.J., and Bish, D.L. (2013) Fitting full X-ray diffraction patterns for quantitative analysis: a method for readily quantifying crystalline and disordered phases. Advances in Materials Physics and Chemistry, 3, 47-53.

Christensen, P.R., Jakosky, B.M., Kieffer, H.H., Malin, M.C., McSween, H.Y., Nealson, K., Mehall, G.L., Silverman, S.H., Ferry, S., Caplinger, M., and Ravine, M. (2004a) The thermal emission imaging system (THEMIS) for the Mars 2001 Odyssey Mission. Space Science Reviews, 110(1-2), 85-130.

Christensen, P.R., Wyatt, M.B., Glotch, T.D., Rogers, A.D., Anwar, S., Arvidson, R.E., Bandfield, J.L., Blaney, D.L., Budney, C., Calvin, W.M., and Fallacaro, A. (2004b) Mineralogy at Meridiani Planum from the Mini-TES experiment on the Opportunity Rover. Science, 306(5702), 1733-1739.

Clark, B.C., Morris, R.V., McLennan, S.M., Gellert, R., Jolliff, B., Knoll, A.H., Squyres, S.W., Lowenstein, T.K., Ming, D.W., Tosca, N.J., and Yen, A. (2005) Chemistry and mineralogy of outcrops at Meridiani Planum. Earth and Planetary Science Letters, 240(1), 73-94.

Dal Negro, A., De Pieri, R., Quareni, S., and Taylor, W.H. (1978) The crystal structures of nine K feldspars from Adamello Massiff (Northern Italy). Acta Crystallographica, B34, 2699-2707.

Dehouck, E., McLennan S.M., Meslin, P.-Y., Cousin, A. (2014) Constraints on abundance, composition, and nature of X-ray amorphous components of soils and rocks at Gale crater, Mars. Journal of Geophysical Research: Planets 119, 2640-2657.

Dera, P., Zhuravlev, K., Prakapenka, V., Rivers, M.L., Finkelstein, G.J., Grubor-Urosevic, O., Tschauner, O., Clark, S.M., and Downs, R.T. (2013) High pressure single-crystal micro X-ray diffraction analysis with GSE_ADA/RSV software. High Pressure Research, 33, 466-484.

Filiberto, J., and Dasgupta, R. (2015) Constraints on the depth and thermal vigor of melting in the Martian mantle. Journal of Geophysical Research: Planets 120, 109-122.

Gellert, R., Clark, B.C. III, MSL and MER Science Teams (2015) Compositional measurements of rocks and soils on NASA's Mars rovers with the alpha-particle X-ray spectrometer (APXS). Elements 11: 39-44.

Golden, D.C., Ming, D.W., Morris, R.V., and Graff, T.G. (2008) Hydrothermal synthesis of hematite spherules and jarosite - Implications for diagenesis and hematite spherule formation in sulphate outcrops at Meridiani Planum, Mars. American Mineralogist, 93, 1201-1214.

Grotzinger, J.P. (2013) Analysis of surface materials by the Curiosity Mars rover. Science, 341, 1475.

Grotzinger, J.P., Sumner, D.Y., Kah, L.C., Stack, K., Gupta, S., Edgar, L., Rubin, D., Lewis, K., Schieber, J., Mangold, N., Milliken, R., Conrad, P.G., DesMarais, D., Farmer, J., Siebach, K., Calef, F., Hurowitz, J., McLennan, S.M., Ming, D., Vaniman, D., Crisp, J., Vasavada, A., Edgett, K.S., Malin, M., Blake, D., Gellert, R., Mahaffy, P., Wiens, R.C., Maurice, S., Grant, J.., Wilson, S., Anderson, Robert C.., Beegle, L.W., Arvidson, R.E., Hallet, B., Sletten, R.S., Rice, M., Bell, J.F., Griffes, J., Ehlmann, B., Anderson, R.B., Bristow, T.F., Dietrich, W.E., Dromart, G., Eigenbrode, J.,

Fraeman, A., Hardgrove, C., Herkenhoff, K., Jandura, L., Kocurek, G., Lee, S., Leshin, L., Leveille, R., Limonadi, D., Maki, J., McCloskey, S., Meyer, M., Minitti, M., Newsom, H., Oehler, D., Okon, A., Palucis, M., Parker, T., Rowland, S., Schmidt, M., Squyres, S., Steele, A., Stolper, E., Summons, R., Treiman, A., Williams, R., and Yingst, A. (2014) A habitable fluvio-lacustrine environment at Yellowknife Bay, Gale crater, Mars. Science, 343(6169), 1242777.

Gupta, A. K. (2015) Origin of Potassium-Rich Silica-Deficient Igneous Rocks. 536, Springer, New York.

Hewins, R.H., Zanda, B., Humayun, M., Nemchin, A., Lorand, J.P., Pont, S., Deldicque, D., Bellucci, J.J., Beck, P., Leroux, H., and Marinova, M. (2017) Regolith breccia Northwest Africa 7533: Mineralogy and petrology with implications for early Mars. Meteoritics & Planetary Science, 52(1), 89-124.

Hurowitz, J.A., Grotzinger, J.P., Fischer, W.W., McLennan, S.M., Milliken, R.E., Stein, N., Vasavada, A.R., Blake, D.F., Dehouck, E., Eigenbrode, J.L., and Fairén, A.G. (2017) Redox stratification of an ancient lake in Gale crater, Mars. Science, 356(6341), 6849.

Klingelhöfer, G., Morris, R.V, Bernhardt, B., Schröder, C., Rodionov, D.S., de Souza, P.A., Yen, A., Gellert, R., Evlanov, E.N., Zubkov, B., and others (2004) Jarosite and hematite at Meridiani Planum from Opportunity's Mössbauer Spectrometer. Science, 306, 1740-5.

Kuehner, S.M., and Joswiak, D.J. (1996) Naturally occurring ferric iron sanidine from the Leucite Hills lamproite. American Mineralogist, 81(1-2), 229-237.

Le Deit., L., Mangold, N., Forni, O., Cousin, A., Lasue, J., Schroder, S., Wiens, R.C., Sumner, D., Fabre, C., Stack, K.M., Anderson, R.B., Blaney, D., Clegg, S., Dromart, G., Fisk, M., Gasnault, O., Grotzinger, J.P., Gupta, S., Lanza, N., Le Mouelic, S., Maurice, S., McLennan, S.M., Meslin, P-Y., Nachon, M., Newsom, H., Payre, V., Rapin, W., Rice, M., Sautter, V., and Treiman, A.H. (2016) The potassic sedimentary rocks in Gale crater, Mars, as seen by ChemCam on board Curiosity. Journal of Geophysical Research: Planets, 121, 784-804.

Lebedeva, Y.S., Pushcharovsky, D.Y., Pasero, M., Merlino, S., Kashaev, A.A., Taroev, V.K., Linthout, K., and Lustenhouwer, W.J. (1993) Ferrian high sanidine in a lamproite from Cancarix, Spain. Mineralogical magazine, 57(2), 289-299.

Lee, C.-T.A., Luffi, P., Plank, T., Dalton, H., and Leeman, W.P. (2009) Constraints on the depths and temperatures of basaltic magma generation on Earth and other terrestrial planets using new thermobarometers for mafic magmas. Earth and Planetary Science Letters 279, 20-33.

Lindsley, D.H. (1983) Pyroxene thermometry. American Mineralogist, 68, 477-493.

McSween, H.Y. and Treiman, A.H. (1998) Martian meteorites. Reviews in Mineralogy and Geochemistry, 36(1), 6-1.

Mills, S.J., Nestola, F., Kahlenberg, V., Christy, A.G., Hejny, C., and Redhammer, G.J. (2013) Looking for jarosite on Mars: the low-temperature crystal structure of jarosite. American Mineralogist, 98, 1966-1971.

Morris, R.V., Klingelhöfer, G., Schröder, C., Fleischer, I., Ming, D.W., Yen, A.S., Gellert, R., Arvidson, R.E., Rodionov, D.S., Crumpler, L.S., Clark, B.C., Cohen, B.A., McCoy, T.J., Mittlefehldt, D.W., Schmidt, M.E., de Souza, P.A., and Squyres, S.W. (2008), Iron mineralogy and aqueous alteration from Husband Hill through Home Plate at Gusev Crater, Mars: results from the Mössbauer instrument on the Spirit Mars Exploration Rover, Journal of Geophysical Research: Planets, 113, E12S42.

Morris, R.V., Klingelhöfer, G., Schröder, C., Rodionov, D.S., Yen, A., Ming, D.W., de Souza, P.A., Wdowiak, T., Fleischer, I., Gellert, R., Bernhardt, B., Bonnes, U., Cohen, B.A., Evlanov, E.N., Foh, J., Gütlich, P., Kankeleit, E., McCoy, T., Mittlefehldt, D.W., Renz, F., Schmidt, M.E., Zubkov, B., Squyres, S.W., Arvidson, R.E. (2006) Mössbauer mineralogy of rock, soil, and dust at Meridiani Planum, Mars: Opportunity's journey across sulfate-rich outcrop, basaltic sand and dust, and hematite lag deposits. Journal of Geophysical Research: Planets, 111.

Morris, R.V., Vaniman, D.T., Blake, D.F., Gellert, R., Chipera, S.J., Rampe, E.B., Ming, D.W., Morrison, S.M., Downs, R.T., Treiman, A.H., Yen, A.S., Grotzinger, J.P., Achilles, C.N., Bristow, T.F., Crisp, J.A., Des Marais, D.J., Farmer, J.D., Fendrich, K.V., Frydenvang, J., Graff, T.G., Morookian, J.M., Stolper, E.M., and Schwenzer, S.P. (2016) Silicic volcanism on Mars evidenced by tridymite in high-SiO_2 sedimentary rock at Gale crater, Proceedings of the National Academy of Sciences, 201607098.

Morrison, S.M., Downs, R.T., Blake, D.F., Vaniman, D.T., Ming, D.W., Rampe, E.B., Bristow, T.F., Achilles, C.N., Chipera, S.J., Yen, A.S., Morris, R.V., Treiman, A.H., Hazen, R.M., Sarrazin, P.C., Gellert, R., Fendrich, K.V., Morookian, J.M., Farmer, J.D., Des Marais, D.J., and Craig, P.I. (2017) Relationships between unit-cell parameters and composition for rock-forming minerals on Earth, Mars, and other extraterrestrial bodies, American Mineralogist (submitted).

Nyquist, L.E., Shih, C.Y., McCubbin, F.M., Santos, A.R., Shearer, C.K., Peng, Z.X., Burger, P.V., and Agee, C.B. (2016) Rb-Sr and Sm-Nd isotopic and REE studies of igneous components in the bulk matrix domain of Martian breccia Northwest Africa 7034. Meteoritics & Planetary Science, 51(3), 483-498.

O'Connell-Cooper, C., L. Thompson, M. Schmidt, and R. Gellert (2017), APXS analysis from the Bagnold dunes, Journal of Geophysical Research (in review).

Papike, J.J., Karner, J.M., Shearer, C.K., and Burger, P. V (2009) Silicate mineralogy of martian meteorites. Geochimica et Cosmochimica Acta, 73, 7443-7485.

Rampe, E.B. Ming, D.W., Blake, D.F., Vaniman, D.T., Chipera, S.J., Bristow, T.F., Morris, R.V., Yen, A.S., Morrison, S.M., Grotzinger, J.P., Peretyazhko, T., Hurowitz, J.A., Siebach, K., Achilles, C.N., Downs, R.T., Farmer, J.D., Fendrich, K.V., Gellert, R., Morookian, J.M., Sarrazin, P., Treiman, A.H., Berger, J., Fairén, A.G., Forni, O., Kah, L., Eigenbrode, J., Lanza, N. L., Sutter, B. (2017) Mineralogical trends in mudstones from the Murray formation, Gale crater, Mars. Earth and Planetary Science Letters, 471, 172-185.

Rampe, E.B., Morris, R. V., Ruff, S.W., Horgan, B., Dehouck, E., Achilles, C.N., Ming, D.W., Bish, D.. L., and Chipera, S.J. (2014) Amorphous phases on the surface of Mars. Eighth International Conference on Mars (2014), 1-2.

Rampe, E.B., Morris, R.V., Archer, P.D., Agresti, D.G., Jr., and Ming, D.W. (2016) Recognizing sulfate and phosphate complexes chemisorbed onto nanophase weathering products on Mars using in-situ and remote observations. American Mineralogist, 101, 678-689.

Ruff, S. W., P. R. Christensen, T. D. Glotch, D. L. Blaney, J. E. Moersch, and M. B. Wyatt (2008) The mineralogy of Gusev crater and Meridiani Planum derived from the Miniature Thermal Emission Spectrometers on the Spirit and Opportunity rovers, in: III, J. F. B. (Ed.), The Martian Surface: Composition, Mineralogy, and Physical Properties. Cambridge University Press, 315-338.

Sack, R.O. (1980) Some constraints on the thermodynamic mixing properties of Fe-Mg orthopyroxenes and olivines. Contributions to Mineralogy and Petrology, 71, 257-269.

Santos, A.R., Agee, C.B., McCubbin, F.M., Shearer, C.K., Burger, P.V., Tartese, R., and Anand, M. (2015) Petrology of igneous clasts in Northwest Africa 7034: Implications for the petrologic diversity of the Martian crust. Geochimica et Cosmochimica Acta, 157, 56-85.

Siebach, K.L., Baker, M.B., Grotzinger, J.P., McLennan, S.M., Gellert, R., Thompson, L.M., and Hurowitz, J.A. (2017) Sorting out compositional trends in sedimentary rocks of the Bradbury group (Aeolis Palus), Gale crater, Mars. Journal of Geophysical Research: Planets, 122(2), 295-328.

Swayze, G.A., Desborough, G.A., Smith, K.S., Lowers, H.A., Hammarstrom, J.M., Diehl, S.F., Leinz, R.W., and Driscoll, R.H. (2008) Understanding jarosite - From mine waste to Mars. Understanding contaminants associated with mineral deposits, In: Verplanck, P.L. (Ed.), Understanding contaminants associated with mineral deposits, U.S.G.S. Circular, 1328, 8-13.

Sutter, B., McAdam, A.C., Mahaffy, P.R., Ming, D.W., Edgett, K.S., Rampe, E.B., Eigenbrode, J.L., Franz, H.B., Freissinet, C., Grotzinger, J.P., and Steele, A. (2017) Evolved Gas Analyses of Sedimentary Rocks and Eolian Sediment in Gale Crater, Mars: Results of the Curiosity Rover's Sample Analysis at Mars (SAM) Instrument from Yellowknife Bay to the Namib Dune. Journal of Geophysical Research: Planets. (accepted - DOI: 10.1002/2016JE005225)

Thompson, L.M., Schmidt, M.E., Spray, J.G., Berger, J.A., Faréin, A., Campbell, J.L., Perrett, G.M., Boyd, N., Gellert, R., Pradler, I., VanBommel, S.J. (2016) Potassium-rich sandstones on Mars, Gale crater: the APXS perspective. Journal of Geophysical Research: Planets, 121, 1980-2003.

Treiman, A.H. and Medard, E. (2016) Mantle metasomatism in Mars: potassic basaltic sandstone in Gale crater derived from partial melt of phlogopite-peridotite. Geological Society of America Abstracts with Programs, 48, 7, 49-12.

Treiman, A.H., Bish, D.L., Vaniman, D.T., Chipera, S.J., Blake, D.F., Ming, D.W., Morris, R. V., Bristow, T.F., Morrison, S.M., Baker, M.B., Rampe, E.B., Downs, R.T., Filiberto, J., Glazner, A.F., Gellert, R., Thompson, L.M., Schmidt, M.E., Le Deit, L., Wiens, R.C., McAdam, A.C., Achilles, C.N., Edgett, K.S., Farmer, J.D., Fendrich, K.V., Grotzinger, J.P., Gupta, S. Morookian, J.M., Newcombe, M.E., Rice, M.S., Spray, J.G., Stolper, E.M., Sumner, D.Y., Vasavada, A.R., and Yen, A.S. (2016) Mineralogy, provenance, and diagenesis of a potassic basaltic sandstone on Mars: CheMin X-ray diffraction of the Windjana sample (Kimberley area, Gale Crater). Journal of Geophysical Research: Planets, 121, 75-106.

Treiman, A.H., Morris, R.V., Agresti, D.G., Graff, T.G., Achilles, C.N., Rampe, E.B., Bristow, T.F., Ming, D.W., Blake, D.F., Bish, D.L., Chipera, S.J., Morrison, S.M., Downs, R.T. (2014) Ferrian saponite from the Santa Monica Mountains (California, U.S.A., Earth): characterization as an analog for clay minerals on Mars with application to Yellowknife Bay in Gale crater, American Mineralogist, 99, 2234-2250.

Turnock, A.C., Lindsley, D.H., and Grover, J.E. (1973) Synthesis and unit cell parameters of Ca-Mg-Fe pyroxenes. American Mineralogist, 58, 50-59.

Vaniman, D.T., Bish, D.L., Ming, D.W., Bristow, T.F., Morris, R.V., Blake, D.F., Chipera, S.J., Morrison, S.M., Treiman, A.H., Rampe, E.B., Rice, M., Achilles, C.N., Grotzinger, J.P., McLennan, S.M., Williams, J., Bell, J.F. III, Newsom, H.E., Downs, R.T., Maurice, S., Sarrazin, P., Yen, A.S., Morookian, J.M., Farmer, J.D., Stack, K., Milliken, R.E., Ehlmann, B.L., Sumner, D.Y., Berger, G., Crisp, J.A., Hurowitz, J.A., Anderson, R., Des Marais, D.J., Stolper, E.M., Edgett, K.S., Gupta, S., Spanovich, N., and MSL Science Team (2014) Mineralogy of a mudstone at Yellowknife Bay, Gale crater, Mars. Science, 343, 1-9.

Watkins, J., Grotzinger, J., Stein, N., Banham, S., Gupta, S., Rubin, D., Stack Morgan, K., Edgett, K., Frydenvang, J., Siebach, K., Lamb, M., Sumner, D., and Lewis, K. (2017) Geometry and significance of an erosional unconformity on Mars, base Stimson formation, Gale crater. Journal of Geophysical Research (submitted).

Wittmann, A., Korotev, R.L., Jolliff, B.L., Irving, A.J., Moser, D.E., Barker, I., and Rumble, D. (2015) Petrography and composition of Martian regolith breccia meteorite Northwest Africa 7475. Meteoritics & Planetary Science, 50(2), 326-352.

Yen, A.S., Ming, D.W., Vaniman, D.T., Gellert, R., Blake, D.F., Morris, R.V., Morrison, S.M., Downs, R.T., Bristow, T.F., Clark, B.C., Chipera, S.J., Farmer, J.D., Grotzinger, J.P., Rampe, E.B., Schimidt, M.E., Sutter, B., Thompson, L.M., Treiman, A.H., and the MSL Science Team (2017) Multiple episodes of aqueous alteration along fractures in mudstone and sandstone in Gale crater, Mars. Earth and Planetary Science Letters, 471, 186-198.

Young, R.A., Ed. (1993) The Rietveld Method, International Union of Crystallography, 298 p. Oxford University Press.

Zolotov, M.Y., and Shock, E.L. (2005) Formation of jarosite-bearing deposits through aqueous oxidation of pyrite at Meridiani Planum, Mars. Geophysical Research Letters, 32, L21203.

This is a preprint, the final version is subject to change, of the American Mineralogist (MSA)
Cite as Authors (Year) Title. American Mineralogist, in press.
DOI: http://dx.doi.org/10.2138/am-2018-6124

TABLES

TABLE 1. Description of Gale crater samples analyzed with CheMin.

Sample	Sol*	Description	Formation
Rocknest	69-93	Wind-blown accumulation of unconsolidated sediment [1]	Soil**
John Klein	182	Fine-grained, homogenous mudstone [2]	Yellowknife Bay
Cumberland	279	Fine-grained, homogenous mudstone [2]	Yellowknife Bay
Windjana	621	Fine-grained, cross-bedded sandstone to siltstone [3]	Kimberley
Confidence Hills	759	Fine-grained mudstone [4]	Murray
Mojave2	882	Fluvial/lacustrine mudstone [4]	Murray
Telegraph Peak	908	Fluvial/lacustrine mudstone [4]	Murray
Buckskin	1060	Finely-laminated mudstone [4,5]	Murray
Big Sky	1119	Unaltered, cross-bedded sandstone [6]	Stimson
Greenhorn	1137	Altered sandstone in a fracture [6]	Stimson
Gobabeb	1280	Active wind-blown dune of unconsolidated sediment [7]	Soil**
Lubango	1320	Altered, cross-bedded sandstone [6]	Stimson
Okoruso	1332	Unaltered, cross-bedded sandstone [6]	Stimson

[1] Bish et al. 2013; Blake et al. 2013 [2] Grotzinger et al. 2014; Vaniman et al. 2014 [3] Treiman et al. 2016; [4] Rampe et al. 2016; [5] Morris et al. 2016; [6] Yen et al. 2016; [7] Achilles et al. 2016.

*Sol sample obtained by Curiosity. Sol is an abbreviation for a solar day on Mars, equivalent to 24 hours, 39 minutes, and 35.244 seconds (Allison 1997).

**Soil comprises globally-derived dust and regional materials.

This is a preprint, the final version is subject to change, of the American Mineralogist (MSA)
Cite as Authors (Year) Title. American Mineralogist, in press.
DOI: http://dx.doi.org/10.2138/am-2018-6124

853 TABLE 2. Refined unit-cell parameters of selected crystalline phases detected with CheMin in Gale crater samples, with 1σ errors.

Phase	Abundance (wt% cryst.)	*a* (Å)	*b* (Å)	*c* (Å)	α (°)	β (°)	γ (°)	*V* (Å^3)
Rocknest								
Plagioclase	40.6(5)	8.168(6)	12.863(6)	7.108(4)	93.46(5)	116.22(3)	90.12(3)	668.4(5)
Olivine	20.7(6)	4.785(3)	10.318(4)	6.025(3)	90	90	90	297.5(2)
Augite	18.1(12)	9.767(22)	8.924(13)	5.263(11)	90	106.47(21)	90	440.0(15)
Pigeonite	12.4(12)	9.651(15)	8.942(18)	5.235(21)	90	108.35(8)	90	428.9(22)
Magnetite	2.8(5)	8.381(4)	8.381(4)	8.381(4)	90	90	90	588.7(3)
Gobabeb								
Plagioclase	36.5(8)	8.181(7)	12.868(7)	7.107(6)	93.49(5)	116.19(4)	90.06(3)	669.8(8)
Olivine	25.8(12)	4.785(3)	10.327(3)	6.033(4)	90	90	90	298.1(3)
Augite	22.0(19)	9.785(15)	8.922(13)	5.276(13)	90	106.45(9)	90	441.8(14)
Pigeonite	10.6(20)	9.675(22)	8.941(27)	5.254(29)	90	108.69(14)	90	430.6(25)
Magnetite	2.1(8)	8.380(8)	8.380(8)	8.380(8)	90	90	90	588.4(4)
John Klein								
Plagioclase	43.5(12)	8.162(5)	12.860(8)	7.108(5)	93.47(5)	116.29(3)	90.10(4)	667.3(8)
Pigeonite	15.9(6)	9.686(20)	8.917(18)	5.208(19)	90	108.57(14)	90	426.5(19)
Orthopyroxene	10.0(12)	18.327(28)	8.964(13)	5.228(7)	90	90	90	859.0(25)
Magnetite	9.2(5)	8.372(2)	8.372(2)	8.372(2)	90	90	90	586.8(2)
Sanidine	4.3(8)	8.551(26)	12.952(30)	7.147(24)	90	115.73(14)	90	713.2(36)
Cumberland								
Plagioclase	42.8(12)	8.162(7)	12.860(8)	7.112(7)	93.42(5)	116.34(4)	90.10(4)	667.5(9)
Pigeonite	17.0(11)	9.680(19)	8.925(20)	5.220(21)	90	108.53(10)	90	427.7(22)
Orthopyroxene	14.5(8)	18.335(20)	8.953(12)	5.239(7)	90	90	90	860.1(22)
Magnetite	11.5(4)	8.369(2)	8.369(2)	8.369(2)	90	90	90	586.3(2)
Sanidine	4.9(7)	8.525(27)	12.973(30)	7.175(27)	90	115.56(18)	90	715.9(39)
Windjana								
Augite	29.3(7)	9.744(9)	8.925(11)	5.258(10)	90	106.36(6)	90	438.7(9)
Sanidine	25.9(12)	8.578(6)	13.016(7)	7.165(7)	90	116.00(6)	90	719.0(10)
Magnetite	16.1(14)	8.373(1)	8.373(1)	8.373(1)	90	90	90	587.0(2)
Pigeonite	12.3(18)	9.648(16)	8.895(29)	5.210(16)	90	108.58(21)	90	423.9(19)
Olivine	7.1(17)	4.773(7)	10.288(9)	6.006(11)	90	90	90	294.9(8)
Plagioclase	5.7(9)	8.172(40)	12.912(81)	7.108(49)	94.35(98)	116.27(45)	89.90(61)	670.1(70)
Confidence Hills								
Plagioclase	38.3(22)	8.166(7)	12.859(7)	7.111(4)	93.44(6)	116.31(4)	90.16(4)	667.8(5)
Sanidine	9.4(1)	8.584(13)	13.009(18)	7.160(15)	90	115.96(13)	90	718.7(18)
Pigeonite	9.9(16)	9.648(25)	8.927(46)	5.207(25)	90	108.60(18)	90	425.1(12)
Magnetite	5.6(7)	8.365(3)	8.365(3)	8.365(3)	90	90	90	585.4(7)
Mojave2								

This is a preprint, the final version is subject to change, of the American Mineralogist (MSA)
Cite as Authors (Year) Title. American Mineralogist, in press.
DOI: http://dx.doi.org/10.2138/am-2018-6124

Plagioclase	55.3(18)	8.164(4)	12.859(3)	7.110(2)	93.50(4)	116.28(1)	90.10(3)	667.8(4)
Pigeonite	10.8(8)	9.670(31)	8.921(44)	5.196(48)	90	108.66(53)	90	424.7(14)
Magnetite	7.1(8)	8.357(2)	8.357(2)	8.357(2)	90	90	90	583.6(3)
Jarosite	7.5(7)	7.268(9)	7.268(9)	16.940(70)	90	90	120	775.0(89)
Telegraph Peak								
Plagioclase	43.9(23)	8.157(3)	12.858(6)	7.111(2)	93.47(2)	116.28(2)	90.08(2)	667.2(4)
Magnetite	13.1(7)	8.355(1)	8.355(1)	8.355(1)	90	90	90	583.3(1)
Sanidine	8.4(18)	8.526(20)	12.986(16)	7.152(15)	90	115.94(17)	90	712.0(16)
Pigeonite	6.8(8)	9.670(40)	8.926(57)	5.194(38)	90	108.62(29)	90	425.0(15)
Buckskin								
Plagioclase	42.7(15)	8.155(3)	12.862(4)	7.106(4)	93.32(2)	116.28(2)	90.10(2)	666.9(7)
Sanidine	8.38(9)	8.54(2)	13.01(2)	7.15(2)	90	115.8(1)	90	715.2(29)
Magnetite	7.0(4)	8.359(1)	8.359(1)	8.359(1)	90	90	90	584.04(8)
Big Sky								
Plagioclase	45.6(11)	8.159(8)	12.875(8)	7.103(7)	93.47(6)	116.09(4)	89.97(5)	668.6(10)
Pigeonite	21.2(9)	9.672(9)	8.886(10)	5.222(9)	90	108.56(4)	90	425.4(10)
Magnetite	12.9(4)	8.389(1)	8.389(1)	8.389(1)	90	90	90	590.3(2)
Orthopyroxene	10.5(11)	18.271(16)	8.986(11)	5.216(5)	90	90	90	856.4(13)
Greenhorn								
Plagioclase	42.1(12)	8.165(7)	12.891(9)	7.108(7)	93.24(7)	116.10(4)	90.06(4)	670.5(10)
Magnetite	17.3(5)	8.387(1)	8.387(1)	8.387(1)	90	90	90	590.0(1)
Orthopyroxene	7.6(10)	18.351(39)	8.957(12)	5.251(10)	90	90	90	863.1(28)
Lubango								
Plagioclase	43.2(12)	8.166(11)	12.891(11)	7.111(9)	93.26(10)	116.21(5)	90.04(6)	670.2(12)
Magnetite	11.1(5)	8.380(3)	8.380(3)	8.380(3)	90	90	90	588.5(5)
Orthopyroxene	10.4(11)	18.328(47)	8.956(19)	5.249(13)	90	90	90	861.8(28)
Pigeonite	5.9(7)	9.673(30)	8.889(27)	5.213(30)	90	108.28(14)	90	425.7(30)
Okoruso								
Plagioclase	41.9(13)	8.160(8)	12.880(7)	7.108(6)	93.59(7)	116.17(4)	89.91(6)	668.9(9)
Pigeonite	20.8(5)	9.667(7)	8.891(8)	5.217(8)	90	108.51(3)	90	425.3(8)
Magnetite	17.3(5)	8.383(1)	8.383(1)	8.383(1)	90	90	90	589.2(1)
Orthopyroxene	11.0(11)	18.310(57)	8.951(45)	5.242(19)	90	90	90	859.1(19)

This is a preprint, the final version is subject to change, of the American Mineralogist (MSA)
Cite as Authors (Year) Title. American Mineralogist, in press.
DOI: http://dx.doi.org/10.2138/am-2018-6124

860 TABLE 3. CheMin sample cell offset distances

CheMin Sample	Offset (μm)	Sample cell
Rocknest	-53	7a
Gobabeb	-38	7a
John Klein	-68	13b
Cumberland	-70	12b
Windjana	-74	13a
Confidence Hills	-74	12a
Mojave 2	-25	6a
Telegraph Peak	-45	5b
Buckskin	-76	14b
Big Sky	-26	7b
Greenhorn	-66	8a
Lubango	-75	8a
Okoruso	-28	7b

*Offset calculated from Oudam2, a later sample analyzed with CheMin in the former Windjana cell, 13a.

861

862 TABLE 4. CheMin plagioclase: empirical chemical formulas and associated errors (1σ).

Sample	Plagioclase Formula
Rocknest	$Ca_{0.49(4)}Na_{0.51(4)}Al_{1.49}Si_{2.51}O_8$
Gobabeb	$Ca_{0.63(6)}Na_{0.37(6)}Al_{1.63}Si_{2.37}O_8$
John Klein	$Ca_{0.40(4)}Na_{0.60(4)}Al_{1.40}Si_{2.60}O_8$
Cumberland	$Ca_{0.33(5)}Na_{0.67(5)}Al_{1.33}Si_{2.67}O_8$
Windjana	$Ca_{0.17(60)}Na_{0.83(60)}Al_{1.17}Si_{2.83}O_8$
Confidence Hills	$Ca_{0.39(4)}Na_{0.61(4)}Al_{1.39}Si_{2.61}O_8$
Mojave2	$Ca_{0.41(3)}Na_{0.59(3)}Al_{1.41}Si_{2.59}O_8$
Telegraph Peak	$Ca_{0.36(3)}Na_{0.64(3)}Al_{1.36}Si_{2.64}O_8$
Buckskin	$Ca_{0.38(3)}Na_{0.62(3)}Al_{1.38}Si_{2.62}O_8$
Big Sky	$Ca_{0.52(5)}Na_{0.48(5)}Al_{1.52}Si_{2.48}O_8$
Greenhorn	$Ca_{0.40(6)}Na_{0.60(6)}Al_{1.40}Si_{2.60}O_8$
Lubango	$Ca_{0.30(8)}Na_{0.70(8)}Al_{1.30}Si_{2.70}O_8$
Okoruso	$Ca_{0.39(5)}Na_{0.61(5)}Al_{1.39}Si_{2.61}O_8$
Average	$Ca_{0.40(11)}Na_{0.60(11)}Al_{1.40}Si_{2.60}O_8$
Soil Average	$Ca_{0.56(8)}Na_{0.44(8)}Al_{1.56}Si_{2.44}O_8$
Yellowknife Bay Average	$Ca_{0.37(5)}Na_{0.63(5)}Al_{1.38}Si_{2.62}O_8$
Murray Average	$Ca_{0.38(2)}Na_{0.62(2)}Al_{1.38}Si_{2.62}O_8$
Stimson Average	$Ca_{0.40(8)}Na_{0.60(8)}Al_{1.40}Si_{2.60}O_8$
Unaltered Stimson Average	$Ca_{0.45(7)}Na_{0.55(7)}Al_{1.45}Si_{2.55}O_8$
Altered Stimson Average	$Ca_{0.35(6)}Na_{0.65(6)}Al_{1.35}Si_{2.65}O_8$

863

This is a preprint, the final version is subject to change, of the American Mineralogist (MSA)
Cite as Authors (Year) Title. American Mineralogist, in press.
DOI: http://dx.doi.org/10.2138/am-2018-6124

TABLE 5. CheMin alkali feldspar: empirical chemical formulas, Si-Al ordering, and associated errors (1σ).

Sample	Phase	Formula	Ordering
John Klein	sanidine	$K_{0.53(18)}Na_{0.47}Al_1Si_3O_8$	0.05(36)
Cumberland	sanidine	$K_{0.77(19)}Na_{0.23}Al_1Si_3O_8$	0.31(40)
Windjana	sanidine	$K_{0.87(5)}Na_{0.13}Al_1Si_3O_8$	-0.07(10)
Confidence Hills	sanidine	$K_{0.82(11)}Na_{0.18}Al_1Si_3O_8$	-0.10(23)
Telegraph Peak	sanidine	$K_{0.69(11)}Na_{0.31}Al_1Si_3O_8$	-0.07(22)
Buckskin	sanidine	$K_{0.76(14)}Na_{0.24}Al_1Si_3O_8$	-0.24(29)
Average		$K_{0.74(17)}Na_{0.26}Al_1Si_3O_8$	-0.02(31)
Yellowknife Bay Average		$K_{0.65(18)}Na_{0.35}Al_1Si_3O_8$	0.18(30)
Murray Average		$K_{0.76(13)}Na_{0.24}Al_1Si_3O_8$	-0.14(26)

TABLE 6. CheMin pigeonite: empirical chemical formulas and associated errors (1σ).

Sample	Pigeonite Formula
Rocknest	$Mg_{0.97(8)}Fe_{1.03(9)}Si_2O_6$
Gobabeb	$Mg_{0.95(12)}Fe_{0.99(17)}Ca_{0.06(8)}Si_2O_6$
John Klein	$Mg_{1.17(10)}Fe_{0.64(14)}Ca_{0.19(6)}Si_2O_6$
Cumberland	$Mg_{1.08(11)}Fe_{0.78(16)}Ca_{0.14(8)}Si_2O_6$
Windjana	$Mg_{1.29(13)}Fe_{0.70(15)}Ca_{0.01(6)}Si_2O_6$
Confidence Hills	$Mg_{1.06(18)}Fe_{0.94(18)}Si_2O_6$
Mojave2	$Mg_{1.10(20)}Fe_{0.83(26)}Ca_{0.07(10)}Si_2O_6$
Telegraph Peak	$Mg_{1.05(23)}Fe_{0.89(30)}Ca_{0.06(13)}Si_2O_6$
Big Sky	$Mg_{1.44(7)}Fe_{0.39(9)}Ca_{0.17(4)}Si_2O_6$
Lubango	$Mg_{1.54(17)}Fe_{0.18(17)}Ca_{0.28(6)}Si_2O_6$
Okoruso	$Mg_{1.39(7)}Fe_{0.48(10)}Ca_{0.13(5)}Si_2O_6$
Average	$Mg_{1.18(19)}Fe_{0.72(26)}Ca_{0.10(9)}Si_2O_6$
Soil Average	$Mg_{0.95(5)}Fe_{1.02(7)}Ca_{0.03(4)}Si_2O_6$
Yellowknife Bay Average	$Mg_{1.13(9)}Fe_{0.71(13)}Ca_{0.16(6)}Si_2O_6$
Murray Average	$Mg_{1.07(7)}Fe_{0.89(9)}Ca_{0.04(4)}Si_2O_6$
Stimson Average	$Mg_{1.45(7)}Fe_{0.35(13)}Ca_{0.19(6)}Si_2O_6$
Unaltered Stimson Average	$Mg_{1.41(4)}Fe_{0.44(6)}Ca_{0.15(3)}Si_2O_6$

This is a preprint, the final version is subject to change, of the American Mineralogist (MSA)
Cite as Authors (Year) Title. American Mineralogist, in press.
DOI: http://dx.doi.org/10.2138/am-2018-6124

874

875 TABLE 7. CheMin augite: empirical chemical formulas and associated errors (1σ).

Sample	Augite Formula
Rocknest	$Mg_{0.94(9)}Ca_{0.72(4)}Fe_{0.34(10)}Si_2O_6$
Gobabeb	$Mg_{0.89(8)}Ca_{0.73(3)}Fe_{0.38(9)}Si_2O_6$
Windjana	$Mg_{1.03(7)}Ca_{0.75(4)}Fe_{0.21(9)}Si_2O_6$
Average	$Mg_{0.96(6)}Ca_{0.73(2)}Fe_{0.31(8)}Si_2O_6$
Soil Average	$Mg_{0.92(5)}Ca_{0.72(2)}Fe_{0.36(5)}Si_2O_6$

876

877

878

879

880

881 TABLE 8. CheMin orthopyroxene: empirical chemical formulas and associated errors (1σ).

Sample	Orthopyroxene Formula
John Klein	$Mg_{0.75(8)}\ Fe_{1.25(8)}Si_2O_6$
Cumberland	$Mg_{0.83(8)}Fe_{1.15(10)}Ca_{0.02(5)}Si_2O_6$
Big Sky	$Mg_{0.69(7)}Fe_{1.31(7)}Si_2O_6$
Greenhorn	$Mg_{0.80(8)}Fe_{1.16(9)}Ca_{0.04(4)}Si_2O_6$
Lubango	$Mg_{0.81(10)}Fe_{1.19(11)}Si_2O_6$
Okoruso	$Mg_{0.86(20)}Fe_{1.14(20)}Si_2O_6$
Average	$Mg_{0.79(6)}Fe_{1.20(6)}Ca_{0.01(2)}Si_2O_6$
Yellowknife Bay Average	$Mg_{0.79(7)}Fe_{1.20(8)}Ca_{0.01(4)}Si_2O_6$
Stimson Average	$Mg_{0.79(7)}Fe_{1.20(7)}Ca_{0.01(2)}Si_2O_6$
Altered Stimson Average	$Mg_{0.80(5)}Fe_{1.17(5)}Ca_{0.03(3)}Si_2O_6$
Unaltered Stimson Average	$Mg_{0.77(11)}Fe_{1.23(11)}Si_2O_6$

882

883

884

885

886 TABLE 9. CheMin olivine: empirical chemical formulas and associated errors (1σ).

Sample	Olivine Formula
Rocknest	$Mg_{1.14(3)}Fe_{0.86(3)}SiO_4$
Gobabeb	$Mg_{1.08(3)}Fe_{0.92(3)}SiO_4$
Windjana	$Mg_{1.35(7)}Fe_{0.65(7)}SiO_4$
Average	$Mg_{1.19(12)}Fe_{0.81}SiO_4$
Soil Average	$Mg_{1.11(4)}Fe_{0.89}SiO_4$

887

This is a preprint, the final version is subject to change, of the American Mineralogist (MSA)
Cite as Authors (Year) Title. American Mineralogist, in press.
DOI: http://dx.doi.org/10.2138/am-2018-6124

888
889
890
891 TABLE 10. CheMin magnetite: empirical chemical formulas and associated errors (1σ).

	$Fe_{3-x}\square_xO_4$		$FeAl_2O_4$		$Fe_{1-x}Al_{2-y}\square_{x+y}O_4$			$(FeMgCr^{3+})_{\Sigma=2}O_4$		
	Fe	□	Fe	Al	Fe	Al	□	Fe	Mg	Cr
Rocknest	2.86(5)	0.14	2.87(4)	0.13	2.76(5)	0.11(6)	0.13(8)	--	--	--
Gobabeb	2.86(6)	0.14	2.86(7)	0.14	2.76(7)	0.11(7)	0.13(9)	--	--	--
John Klein	2.82(5)	0.18	2.79(3)	0.21	2.71(4)	0.14(6)	0.16(7)	0.89(5)	0.11(5)	2.00(7)
Cumberland	2.81(5)	0.19	2.77(3)	0.23	2.69(4)	0.15(6)	0.16(7)	0.82(5)	0.18(5)	2.00(7)
Windjana	2.83(5)	0.17	2.80(2)	0.20	2.71(4)	0.14(6)	0.15(7)	0.91(3)	0.09(3)	2.00(5)
Confidence hills	2.79(5)	0.21	2.74(3)	0.26	2.66(5)	0.16(6)	0.18(8)	0.73(7)	0.27(7)	2.00(10)
Mojave2	2.76(5)	0.24	2.67(3)	0.33	2.61(4)	0.19(6)	0.20(7)	0.55(5)	0.45(5)	2.00(7)
Telegraph Peak	2.75(5)	0.25	2.65(2)	0.35	2.60(4)	0.20(6)	0.20(7)	0.51(3)	0.49(3)	2.00(5)
Buckskin	2.77(5)	0.23	2.69(2)	0.31	2.62(4)	0.19(6)	0.19(7)	0.60(3)	0.40(3)	2.00(5)
Big Sky	2.90(5)	0.10	2.93(2)	0.07	2.82(4)	0.08(6)	0.11(7)	--	--	--
Greenhorn	2.89(5)	0.11	2.92(2)	0.08	2.80(4)	0.08(6)	0.11(7)	--	--	--
Lubango	2.86(5)	0.14	2.86(3)	0.14	2.76(5)	0.11(6)	0.13(8)	--	--	--
Okoruso	2.87(5)	0.13	2.89(2)	0.11	2.78(4)	0.10(6)	0.12(7)	--	--	--
Average	2.83(5)	0.17	2.80(9)	0.20	2.71(7)	0.14(4)	0.15(3)	0.72(15)	0.28(15)	2.00(1)
Soil Average	2.86(3)	0.14	2.86(3)	0.14	2.76(3)	0.11(3)	0.13(4)	--	--	--
Yellowknife Bay Average	2.82(4)	0.18	2.78(2)	0.22	2.70(3)	0.14(4)	0.16(5)	0.60(8)	0.40(8)	2.00(2)
Murray Average	2.77(2)	0.23	2.69(4)	0.31	2.62(3)	0.19(2)	0.19(2)	0.60(8)	0.40(8)	2.00(2)
Stimson Average	2.88(2)	0.12	2.90(3)	0.10	2.79(3)	0.09(2)	0.12(2)	--	--	--
Unaltered Stimson Average	2.88(3)	0.12	2.91(3)	0.09	2.79(3)	0.09(3)	0.12(4)	--	--	--
Altered Stimson Average	2.87(3)	0.13	2.89(3)	0.11	2.78(3)	0.10(3)	0.12(4)	--	--	--

892

893

894

895

This is a preprint, the final version is subject to change, of the American Mineralogist (MSA)
Cite as Authors (Year) Title. American Mineralogist, in press.
DOI: http://dx.doi.org/10.2138/am-2018-6124

TABLE 11. CheMin sample crystalline mineral phases (oxide wt%) and their relative abundance (wt%).

Rocknest	CaO	MgO	FeO	Fe_2O_3	SiO_2	Na_2O	Al_2O_3	TiO_2	K_2O	SO_3	H_2O	P_2O_5	F	Abund
augite	18.058	17.050	10.965	0.000	53.927	0.000	0.000	0.000	0.000	0.000	0.000	0.000	0.000	0.181
olivine	0.000	27.383	36.818	0.000	35.799	0.000	0.000	0.000	0.000	0.000	0.000	0.000	0.000	0.207
plagioclase	10.075	0.000	0.000	0.000	55.974	5.912	28.039	0.000	0.000	0.000	0.000	0.000	0.000	0.406
pigeonite	0.000	16.733	31.766	0.000	51.501	0.000	0.000	0.000	0.000	0.000	0.000	0.000	0.000	0.124
magnetite	0.000	0.000	18.879	81.121	0.000	0.000	0.000	0.000	0.000	0.000	0.000	0.000	0.000	0.028
hematite	0.000	0.000	0.000	100.00	0.000	0.000	0.000	0.000	0.000	0.000	0.000	0.000	0.000	0.015
ilmenite	0.000	0.000	47.350	0.000	0.000	0.000	0.000	52.650	0.000	0.000	0.000	0.000	0.000	0.014
quartz	0.000	0.000	0.000	0.000	100.000	0.000	0.000	0.000	0.000	0.000	0.000	0.000	0.000	0.012
anhydrite	41.190	0.000	0.000	0.000	0.000	0.000	0.000	0.000	0.000	58.810	0.000	0.000	0.000	0.013
Total	7.895	10.829	14.737	3.771	47.483	2.400	11.384	0.737	0.000	0.765	0.000	0.000	0.000	
Gobabeb	CaO	MgO	FeO	Fe_2O_3	SiO_2	Na_2O	Al_2O_3	TiO_2	K_2O	SO_3	H_2O	P_2O_5	F	Abund
augite	18.149	16.046	12.225	0.000	53.580	0.000	0.000	0.000	0.000	0.000	0.000	0.000	0.000	0.220
olivine	0.000	25.652	38.948	0.000	35.400	0.000	0.000	0.000	0.000	0.000	0.000	0.000	0.000	0.258
plagioclase	13.045	0.000	0.000	0.000	52.211	4.171	30.573	0.000	0.000	0.000	0.000	0.000	0.000	0.365
pigeonite	1.373	16.259	30.861	0.000	51.508	0.000	0.000	0.000	0.000	0.000	0.000	0.000	0.000	0.106
magnetite	0.000	0.000	18.482	81.518	0.000	0.000	0.000	0.000	0.000	0.000	0.000	0.000	0.000	0.021
hematite	0.000	0.000	0.000	100.00	0.000	0.000	0.000	0.000	0.000	0.000	0.000	0.000	0.000	0.009
quartz	0.000	0.000	0.000	0.000	100.000	0.000	0.000	0.000	0.000	0.000	0.000	0.000	0.000	0.008
anhydrite	41.190	0.000	0.000	0.000	0.000	0.000	0.000	0.000	0.000	58.810	0.000	0.000	0.000	0.013
Total	9.435	11.872	16.398	2.612	46.238	1.523	11.159	0.000	0.000	0.765	0.000	0.000	0.000	
John Klein	CaO	MgO	FeO	Fe_2O_3	SiO_2	Na_2O	Al_2O_3	TiO_2	K_2O	SO_3	H_2O	P_2O_5	F	Abund
olivine‡	0.000	27.383	36.818	0.000	35.799	0.000	0.000	0.000	0.000	0.000	0.000	0.000	0.000	0.080
plagioclase	8.435	0.000	0.000	0.000	58.052	6.874	26.639	0.000	0.000	0.000	0.000	0.000	0.000	0.435
pigeonite	4.820	20.961	20.594	0.000	53.625	0.000	0.000	0.000	0.000	0.000	0.000	0.000	0.000	0.158
orthopyroxene	0.000	12.671	37.275	0.000	50.054	0.000	0.000	0.000	0.000	0.000	0.000	0.000	0.000	0.100
magnetite	0.000	0.000	15.275	84.725	0.000	0.000	0.000	0.000	0.000	0.000	0.000	0.000	0.000	0.092
hematite	0.000	0.000	0.000	100.00	0.000	0.000	0.000	0.000	0.000	0.000	0.000	0.000	0.000	0.013
akaganeite	0.000	0.000	88.860	0.000	0.000	0.000	0.000	0.000	0.000	0.000	11.140	0.000	0.000	0.010
sanidine	0.000	0.000	0.000	0.000	66.574	5.383	18.827	0.000	9.216	0.000	0.000	0.000	0.000	0.043
bassanite	38.514	0.000	0.000	0.000	0.000	0.000	0.000	0.000	0.000	55.143	6.343	0.000	0.000	0.027
anhydrite	41.190	0.000	0.000	0.000	0.000	0.000	0.000	0.000	0.000	58.810	0.000	0.000	0.000	0.042
Total	7.201	6.769	12.221	9.095	44.457	3.222	12.397	0.000	0.396	3.959	0.283	0.000	0.000	
Cumberland	CaO	MgO	FeO	Fe_2O_3	SiO_2	Na_2O	Al_2O_3	TiO_2	K_2O	SO_3	H_2O	P_2O_5	F	Abund
olivine‡	0.000	27.383	36.818	0.000	35.799	0.000	0.000	0.000	0.000	0.000	0.000	0.000	0.000	0.033
plagioclase	6.808	0.000	0.000	0.000	60.114	7.828	25.250	0.000	0.000	0.000	0.000	0.000	0.000	0.428
pigeonite	3.357	19.225	24.600	0.000	52.819	0.000	0.000	0.000	0.000	0.000	0.000	0.000	0.000	0.170
orthopyroxene	0.416	14.038	34.952	0.000	50.594	0.000	0.000	0.000	0.000	0.000	0.000	0.000	0.000	0.145
magnetite	0.000	0.000	14.059	85.941	0.000	0.000	0.000	0.000	0.000	0.000	0.000	0.000	0.000	0.115
hematite	0.000	0.000	0.000	100.00	0.000	0.000	0.000	0.000	0.000	0.000	0.000	0.000	0.000	0.008
akaganeite	0.000	0.000	88.860	0.000	0.000	0.000	0.000	0.000	0.000	0.000	11.140	0.000	0.000	0.016
sanidine	0.000	0.000	0.000	0.000	65.635	2.592	18.561	0.000	13.212	0.000	0.000	0.000	0.000	0.049
bassanite	38.514	0.000	0.000	0.000	0.000	0.000	0.000	0.000	0.000	55.143	6.343	0.000	0.000	0.023
anhydrite	41.190	0.000	0.000	0.000	0.000	0.000	0.000	0.000	0.000	58.810	0.000	0.000	0.000	0.013
Total	4.955	6.209	13.522	10.714	46.425	3.475	11.710	0.000	0.646	2.017	0.328	0.000	0.000	
Windjana	CaO	MgO	FeO	Fe_2O_3	SiO_2	Na_2O	Al_2O_3	TiO_2	K_2O	SO_3	H_2O	P_2O_5	F	Abund
augite	19.286	18.983	6.958	0.000	54.773	0.000	0.000	0.000	0.000	0.000	0.000	0.000	0.000	0.292
olivine	0.000	33.759	28.971	0.000	37.270	0.000	0.000	0.000	0.000	0.000	0.000	0.000	0.000	0.070
plagioclase	2.892	0.000	0.000	0.000	65.077	10.124	21.907	0.000	0.000	0.000	0.000	0.000	0.000	0.056
pigeonite	0.301	23.310	22.505	0.000	53.883	0.000	0.000	0.000	0.000	0.000	0.000	0.000	0.000	0.123
magnetite	0.000	0.000	15.679	84.321	0.000	0.000	0.000	0.000	0.000	0.000	0.000	0.000	0.000	0.161
hematite	0.000	0.000	0.000	100.00	0.000	0.000	0.000	0.000	0.000	0.000	0.000	0.000	0.000	0.017
akaganeite	0.000	0.000	88.860	0.000	0.000	0.000	0.000	0.000	0.000	0.000	11.140	0.000	0.000	0.007
sanidine	0.000	0.000	0.000	0.000	65.237	1.409	18.448	0.000	14.906	0.000	0.000	0.000	0.000	0.259
bassanite	38.514	0.000	0.000	0.000	0.000	0.000	0.000	0.000	0.000	55.143	6.343	0.000	0.000	0.007
anhydrite	41.190	0.000	0.000	0.000	0.000	0.000	0.000	0.000	0.000	58.810	0.000	0.000	0.000	0.008
Total	6.430	10.773	9.974	15.276	45.771	0.932	6.005	0.000	3.861	0.856	0.122	0.000	0.000	
Confidence Hills	CaO	MgO	FeO	Fe_2O_3	SiO_2	Na_2O	Al_2O_3	TiO_2	K_2O	SO_3	H_2O	P_2O_5	F	Abund
augite*	18.058	17.050	10.965	0.000	53.927	0.000	0.000	0.000	0.000	0.000	0.000	0.000	0.000	0.120
olivine	0.000	57.294	0.000	0.000	42.706	0.000	0.000	0.000	0.000	0.000	0.000	0.000	0.000	0.023
plagioclase	8.044	0.000	0.000	0.000	58.548	7.103	26.305	0.000	0.000	0.000	0.000	0.000	0.000	0.383
pigeonite	0.000	18.545	29.308	0.000	52.147	0.000	0.000	0.000	0.000	0.000	0.000	0.000	0.000	0.099
orthopyroxene	0.000	17.349	30.926	0.000	51.726	0.000	0.000	0.000	0.000	0.000	0.000	0.000	0.000	0.039
magnetite	0.000	0.000	12.423	87.577	0.000	0.000	0.000	0.000	0.000	0.000	0.000	0.000	0.000	0.056
hematite	0.000	0.000	0.000	100.00	0.000	0.000	0.000	0.000	0.000	0.000	0.000	0.000	0.000	0.128

This is a preprint, the final version is subject to change, of the American Mineralogist (MSA)
Cite as Authors (Year) Title. American Mineralogist, in press.
DOI: http://dx.doi.org/10.2138/am-2018-6124

sanidine	0.000	0.000	0.000	0.000	65.447	2.034	18.508	0.000	14.011	0.000	0.000	0.000	0.000	0.094
quartz	0.000	0.000	0.000	0.000	100.000	0.000	0.000	0.000	0.000	0.000	0.000	0.000	0.000	0.013
fluorapatite	54.730	0.000	0.000	0.000	0.000	0.000	0.000	0.000	0.000	0.000	0.000	41.561	3.708	0.024
jarosite	0.000	0.000	0.000	47.830	0.000	0.000	0.000	0.000	9.404	31.974	10.792	0.000	0.000	0.021
Total	6.583	5.891	6.148	18.674	44.553	2.911	11.811	0.000	1.508	0.660	0.223	1.014	0.090	
Mojave2	CaO	MgO	FeO	Fe_2O_3	SiO_2	Na_2O	Al_2O_3	TiO_2	K_2O	SO_3	H_2O	P_2O_5	F	Abund
augite*	18.058	17.050	10.965	0.000	53.927	0.000	0.000	0.000	0.000	0.000	0.000	0.000	0.000	0.053
olivine	0.000	57.294	0.000	0.000	42.706	0.000	0.000	0.000	0.000	0.000	0.000	0.000	0.000	0.006
plagioclase	8.484	0.000	0.000	0.000	57.990	6.845	26.681	0.000	0.000	0.000	0.000	0.000	0.000	0.553
pigeonite	1.748	19.376	26.210	0.000	52.666	0.000	0.000	0.000	0.000	0.000	0.000	0.000	0.000	0.108
magnetite	0.000	0.000	9.110	90.890	0.000	0.000	0.000	0.000	0.000	0.000	0.000	0.000	0.000	0.071
hematite	0.000	0.000	0.000	100.00	0.000	0.000	0.000	0.000	0.000	0.000	0.000	0.000	0.000	0.071
quartz	0.000	0.000	0.000	0.000	100.000	0.000	0.000	0.000	0.000	0.000	0.000	0.000	0.000	0.020
fluorapatite	54.730	0.000	0.000	0.000	0.000	0.000	0.000	0.000	0.000	0.000	0.000	41.561	3.708	0.042
jarosite	0.000	0.000	0.000	44.242	0.000	3.140	3.372	0.000	4.966	33.105	11.174	0.000	0.000	0.075
Total	8.136	3.340	4.059	16.871	42.871	4.021	15.007	0.000	0.372	2.483	0.838	1.746	0.156	
Telegraph Peak	CaO	MgO	FeO	Fe_2O_3	SiO_2	Na_2O	Al_2O_3	TiO_2	K_2O	SO_3	H_2O	P_2O_5	F	Abund
olivine	0.000	28.554	35.372	0.000	36.074	0.000	0.000	0.000	0.000	0.000	0.000	0.000	0.000	0.018
plagioclase	7.478	0.000	0.000	0.000	59.266	7.435	25.821	0.000	0.000	0.000	0.000	0.000	0.000	0.438
pigeonite	1.399	18.507	27.781	0.000	52.312	0.000	0.000	0.000	0.000	0.000	0.000	0.000	0.000	0.068
orthopyroxene	0.000	17.349	30.926	0.000	51.726	0.000	0.000	0.000	0.000	0.000	0.000	0.000	0.000	0.055
magnetite	0.000	0.000	8.272	91.728	0.000	0.000	0.000	0.000	0.000	0.000	0.000	0.000	0.000	0.131
hematite	0.000	0.000	0.000	100.00	0.000	0.000	0.000	0.000	0.000	0.000	0.000	0.000	0.000	0.018
sanidine	0.000	0.000	0.000	0.000	65.959	3.555	18.653	0.000	11.833	0.000	0.000	0.000	0.000	0.084
quartz	0.000	0.000	0.000	0.000	100.000	0.000	0.000	0.000	0.000	0.000	0.000	0.000	0.000	0.014
cristobalite	0.000	0.000	0.000	0.000	100.000	0.000	0.000	0.000	0.000	0.000	0.000	0.000	0.000	0.118
fluorapatite	54.730	0.000	0.000	0.000	0.000	0.000	0.000	0.000	0.000	0.000	0.000	41.561	3.708	0.031
jarosite	0.000	0.000	0.000	47.830	0.000	0.000	0.000	0.000	9.404	31.974	10.792	0.000	0.000	0.024
Total	5.067	2.727	5.310	14.964	51.750	3.555	12.877	0.000	1.220	0.767	0.259	1.288	0.115	
Buckskin	CaO	MgO	FeO	Fe_2O_3	SiO_2	Na_2O	Al_2O_3	TiO_2	K_2O	SO_3	H_2O	P_2O_5	F	Abund
plagioclase	8.073	0.000	0.000	0.000	58.511	7.086	26.330	0.000	0.000	0.000	0.000	0.000	0.000	0.427
magnetite	0.000	0.000	9.944	90.056	0.000	0.000	0.000	0.000	0.000	0.000	0.000	0.000	0.000	0.070
sanidine	0.000	0.000	0.000	0.000	65.654	2.650	18.566	0.000	13.130	0.000	0.000	0.000	0.000	0.084
cristobalite	0.000	0.000	0.000	0.000	100.000	0.000	0.000	0.000	0.000	0.000	0.000	0.000	0.000	0.060
tridymite	0.000	0.000	0.000	0.000	100.000	0.000	0.000	0.000	0.000	0.000	0.000	0.000	0.000	0.341
anhydrite	41.190	0.000	0.000	0.000	0.000	0.000	0.000	0.000	0.000	58.810	0.000	0.000	0.000	0.018
Total	4.188	0.000	0.695	6.291	70.616	3.249	12.803	0.000	1.101	1.056	0.000	0.000	0.000	
Big Sky†	CaO	MgO	FeO	Fe_2O_3	SiO_2	Na_2O	Al_2O_3	TiO_2	K_2O	SO_3	H_2O	P_2O_5	F	Abund
plagioclase	10.754	0.000	0.000	0.000	55.114	5.514	28.618	0.000	0.000	0.000	0.000	0.000	0.000	0.457
pigeonite	4.361	26.815	13.173	0.000	55.652	0.000	0.000	0.000	0.000	0.000	0.000	0.000	0.000	0.202
orthopyroxene	0.000	7.094	44.835	0.000	48.071	0.000	0.000	0.000	0.000	0.000	0.000	0.000	0.000	0.100
magnetite	0.000	0.000	22.024	77.976	0.000	0.000	0.000	0.000	0.000	0.000	0.000	0.000	0.000	0.126
hematite	0.000	0.000	0.000	100.00	0.000	0.000	0.000	0.000	0.000	0.000	0.000	0.000	0.000	0.036
K-feldspar	0.000	0.000	0.000	0.000	64.762	0.000	18.317	0.000	16.922	0.000	0.000	0.000	0.000	0.017
quartz	0.000	0.000	0.000	0.000	100.000	0.000	0.000	0.000	0.000	0.000	0.000	0.000	0.000	0.016
tridymite	0.000	0.000	0.000	0.000	100.000	0.000	0.000	0.000	0.000	0.000	0.000	0.000	0.000	0.018
fluorapatite	54.730	0.000	0.000	0.000	0.000	0.000	0.000	0.000	0.000	0.000	0.000	41.561	3.708	0.013
anhydrite	41.190	0.000	0.000	0.000	0.000	0.000	0.000	0.000	0.000	58.810	0.000	0.000	0.000	0.015
Total	7.125	6.126	9.919	13.425	45.737	2.520	13.390	0.000	0.288	0.882	0.000	0.540	0.048	
Greenhorn	CaO	MgO	FeO	Fe_2O_3	SiO_2	Na_2O	Al_2O_3	TiO_2	K_2O	SO_3	H_2O	P_2O_5	F	Abund
plagioclase	7.874	0.000	0.000	0.000	58.763	7.203	26.160	0.000	0.000	0.000	0.000	0.000	0.000	0.421
pigeonite**	7.439	29.446	6.132	0.000	56.983	0.000	0.000	0.000	0.000	0.000	0.000	0.000	0.000	0.047
orthopyroxene	1.040	13.541	34.923	0.000	50.497	0.000	0.000	0.000	0.000	0.000	0.000	0.000	0.000	0.076
magnetite	0.000	0.000	21.242	78.758	0.000	0.000	0.000	0.000	0.000	0.000	0.000	0.000	0.000	0.173
hematite	0.000	0.000	0.000	100.00	0.000	0.000	0.000	0.000	0.000	0.000	0.000	0.000	0.000	0.060
bassanite	38.514	0.000	0.000	0.000	0.000	0.000	0.000	0.000	0.000	55.143	6.343	0.000	0.000	0.040
quartz	0.000	0.000	0.000	0.000	100.000	0.000	0.000	0.000	0.000	0.000	0.000	0.000	0.000	0.022
anhydrite	41.190	0.000	0.000	0.000	0.000	0.000	0.000	0.000	0.000	58.810	0.000	0.000	0.000	0.161
Total	11.916	2.413	6.617	19.625	33.455	3.032	11.013	0.000	0.000	11.674	0.254	0.000	0.000	
Lubango	CaO	MgO	FeO	Fe_2O_3	SiO_2	Na_2O	Al_2O_3	TiO_2	K_2O	SO_3	H_2O	P_2O_5	F	Abund
plagioclase	5.742	0.000	0.000	0.000	61.466	8.453	24.340	0.000	0.000	0.000	0.000	0.000	0.000	0.432
pigeonite	7.439	29.446	6.132	0.000	56.983	0.000	0.000	0.000	0.000	0.000	0.000	0.000	0.000	0.059
orthopyroxene	0.085	13.639	35.866	0.000	50.410	0.000	0.000	0.000	0.000	0.000	0.000	0.000	0.000	0.104
magnetite	0.000	0.000	18.482	81.518	0.000	0.000	0.000	0.000	0.000	0.000	0.000	0.000	0.000	0.111
hematite	0.000	0.000	0.000	100.00	0.000	0.000	0.000	0.000	0.000	0.000	0.000	0.000	0.000	0.023
bassanite	38.514	0.000	0.000	0.000	0.000	0.000	0.000	0.000	0.000	55.143	6.343	0.000	0.000	0.090
gypsum	32.571	0.000	0.000	0.000	0.000	0.000	0.000	0.000	0.000	46.502	20.927	0.000	0.000	0.023

This is a preprint, the final version is subject to change, of the American Mineralogist (MSA)
Cite as Authors (Year) Title. American Mineralogist, in press.
DOI: http://dx.doi.org/10.2138/am-2018-6124

quartz	0.000	0.000	0.000	0.000	100.000	0.000	0.000	0.000	0.000	0.000	0.000	0.000	0.000	0.035
anhydrite	41.190	0.000	0.000	0.000	0.000	0.000	0.000	0.000	0.000	58.810	0.000	0.000	0.000	0.123
Total	12.210	3.156	6.143	11.349	38.658	3.652	10.515	0.000	0.000	13.266	1.052	0.000	0.000	
Okoruso	CaO	MgO	FeO	Fe_2O_3	SiO_2	Na_2O	Al_2O_3	TiO_2	K_2O	SO_3	H_2O	P_2O_5	F	Abund
plagioclase	8.027	0.000	0.000	0.000	58.570	7.113	26.290	0.000	0.000	0.000	0.000	0.000	0.000	0.419
pigeonite	3.394	25.632	15.867	0.000	55.106	0.000	0.000	0.000	0.000	0.000	0.000	0.000	0.000	0.208
orthopyroxene	0.000	14.568	34.702	0.000	50.730	0.000	0.000	0.000	0.000	0.000	0.000	0.000	0.000	0.110
magnetite	0.000	0.000	19.670	80.330	0.000	0.000	0.000	0.000	0.000	0.000	0.000	0.000	0.000	0.173
hematite	0.000	0.000	0.000	100.00	0.000	0.000	0.000	0.000	0.000	0.000	0.000	0.000	0.000	0.011
K-feldspar	0.000	0.000	0.000	0.000	64.762	0.000	18.317	0.000	16.922	0.000	0.000	0.000	0.000	0.029
bassanite	38.514	0.000	0.000	0.000	0.000	0.000	0.000	0.000	0.000	55.143	6.343	0.000	0.000	0.012
quartz	0.000	0.000	0.000	0.000	100.000	0.000	0.000	0.000	0.000	0.000	0.000	0.000	0.000	0.014
fluorapatite	54.730	0.000	0.000	0.000	0.000	0.000	0.000	0.000	0.000	0.000	0.000	41.561	3.708	0.016
anhydrite	41.190	0.000	0.000	0.000	0.000	0.000	0.000	0.000	0.000	58.810	0.000	0.000	0.000	0.008
Total	5.737	6.934	10.521	14.997	44.861	2.980	11.547	0.000	0.491	1.132	0.076	0.665	0.059	

*Rocknest augite composition was used for Mojave and Confidence Hills because the abundance in the latter samples was too near the instrument detection limit to refine accurate unit-cell parameters.

**Lubango pigeonite composition was used for Greenhorn because the abundance in Greenhorn was too near the detection limited to refine accurate unit-cell parameters. Greenhorn and Lubango represent altered Stimson formation.

†Raw Big Sky crystalline abundances (Yen et al. 2017) were used for the amorphous calculations rather than the contamination-subtracted abundances reported in Table 2.

‡The olivine phase in John Klein and Cumberland is likely due in part, if not entirely, to contamination from Rocknest (Vaniman et al. 2014). Therefore, we use the Rocknest olivine composition in calculations of the bulk crystalline material.

TABLE 12A-E. CheMin sample APXS, amorphous (normalized), and crystalline (normalized) compositions, in oxide wt%. All normalized sums total 100 wt%. The proportion is the minimum (lower limit) of amorphous material and maximum (upper limit) of crystalline material in a sample, based on mass-balance.

TABLE 12A. Martian soil samples.

	Rocknest			Gobabeb			Soil Average		
	APXS	**Xtal**	**Amorph**	**APXS**	**Xtal**	**Amorph**	**APXS**	**Xtal**	**Amorph**
SiO_2	42.970	47.663	24.420	47.880	46.359	50.583	45.425	47.011	37.502
TiO_2	1.190	0.740	3.003	0.880	0.000	2.420	1.035	0.370	2.711
Al_2O_3	9.370	11.427	1.179	9.780	11.188	7.326	9.575	11.308	4.253
Cr_2O_3	0.490	0.000	2.458	0.390	0.000	1.072	0.440	0.000	1.765
FeO_T	19.180	18.199	23.237	17.910	18.797	16.375	18.545	18.498	19.806
MnO	0.424	0.000	2.126	0.367	0.000	1.009	0.395	0.000	1.568
MgO	8.690	10.870	0.000	7.570	11.903	0.000	8.130	11.387	0.000
CaO	7.260	7.925	4.640	7.300	9.460	3.530	7.280	8.692	4.085
Na_2O	2.700	2.409	3.883	2.750	1.527	4.892	2.725	1.968	4.387
K_2O	0.490	0.000	2.458	0.490	0.000	1.347	0.490	0.000	1.903
P_2O_5	0.950	0.000	4.766	0.790	0.000	2.172	0.870	0.000	3.469
SO_3	5.470	0.767	24.366	3.360	0.767	7.898	4.415	0.767	16.132
Cl	0.690	0.000	3.462	0.500	0.000	1.375	0.595	0.000	2.418
F	--	--	--	--	--	--	--	--	--
H_2O	--	--	--	--	--	--	--	--	--
Proportion*	--	0.80246	0.19754	--	0.63764	0.36236		0.72005	0.27995

This is a preprint, the final version is subject to change, of the American Mineralogist (MSA)
Cite as Authors (Year) Title. American Mineralogist, in press.
DOI: http://dx.doi.org/10.2138/am-2018-6124

*These proportions represent the maximum possible proportion of crystalline material (upper limit) and, consequently, the minimum proportion of amorphous material (lower limit). Bulk crystalline and amorphous component compositions computed with FULLPAT-estimated proportions are reported in Achilles et al. (2017).

TABLE 12B. Yellowknife Bay and the Kimberley formations.

	John Klein			Cumberland			Windjana		
	APXS	**Xtal**	**Amorph**	**APXS**	**Xtal**	**Amorph**	**APXS**	**Xtal**	**Amorph**
SiO_2	41.060	44.866	33.007	41.130	46.929	25.557	37.380	46.482	3.614
TiO_2	1.050	0.000	3.287	0.990	0.000	3.659	1.070	0.000	5.174
Al_2O_3	8.510	12.511	0.000	8.630	11.837	0.000	5.620	6.098	3.936
Cr_2O_3	0.470	0.000	1.471	0.460	0.000	1.700	0.490	0.000	2.369
FeO_T	20.680	20.592	20.894	21.950	23.414	18.033	27.900	24.088	43.116
MnO	0.325	0.000	1.018	0.294	0.000	1.086	0.552	0.000	2.667
MgO	8.970	6.832	13.535	9.320	6.276	17.534	12.290	10.941	17.735
CaO	7.870	7.267	9.164	6.660	5.009	11.119	5.260	6.530	0.552
Na_2O	2.930	3.251	2.250	3.010	3.513	1.658	0.960	0.946	1.036
K_2O	0.550	0.400	0.870	0.620	0.653	0.532	3.090	3.921	0.000
P_2O_5	0.920	0.000	2.880	0.860	0.000	3.179	0.640	0.000	3.095
SO_3	5.910	3.995	9.995	4.610	2.039	11.544	3.570	0.870	13.949
Cl	0.520	0.000	1.628	1.190	0.000	4.398	0.570	0.000	2.756
F	--	--	0.000	--	--	0.000	--	--	0.000
H_2O	--	0.285	--	--	0.331	--	--	0.124	--
Proportion *	--	0.68643	0.31357	--	0.737	0.263	--	0.80035	0.19965

*These proportions represent the maximum possible proportion of crystalline material (upper limit) and, consequently, the minimum proportion of amorphous material (lower limit).

This is a preprint, the final version is subject to change, of the American Mineralogist (MSA)
Cite as Authors (Year) Title. American Mineralogist, in press.
DOI: http://dx.doi.org/10.2138/am-2018-6124

TABLE 12C. Murray formation samples.

	Confidence Hills			Mojave2			Telegraph Peak			Buckskin			Murr	
	APXS	**Xtal**	**Amorph**	**APXS**	**Xtal**	**Amorph**	**APXS**	**Xtal**	**Amorph**	**APXS**	**Xtal**	**Amorph**	**APXS**	
SiO_2	48.130	45.372	53.230	49.480	43.652	55.725	52.700	52.592	52.986	73.650	71.064	75.934	55.990	5
TiO_2	1.130	0.000	3.135	1.190	0.000	2.487	1.230	0.000	5.859	1.570	0.000	2.810	1.280	0
Al_2O_3	9.730	12.028	5.708	11.430	15.281	7.196	10.740	13.086	1.881	5.660	12.884	0.000	9.390	1
Cr_2O_3	0.390	0.000	1.082	0.370	0.000	0.773	0.360	0.000	1.715	0.100	0.000	0.179	0.305	0
FeO_T	19.830	23.373	13.652	16.110	19.590	12.269	18.680	19.080	17.129	5.490	6.396	4.796	15.028	1
MnO	0.372	0.000	1.032	0.397	0.000	0.831	0.248	0.000	1.183	0.090	0.000	0.161	0.277	0
MgO	5.550	6.000	4.780	4.550	3.401	5.794	2.930	2.771	3.522	0.820	0.000	1.467	3.463	3
CaO	4.580	6.704	0.843	4.330	8.285	0.000	4.370	5.149	1.425	3.050	4.215	2.145	4.083	6
Na_2O	2.650	2.965	2.105	3.010	4.094	1.819	3.340	3.613	2.304	2.080	3.270	1.152	2.770	3
K_2O	0.980	1.536	0.000	0.730	0.379	1.111	0.980	1.240	0.000	0.960	1.108	0.847	0.913	1
P_2O_5	1.020	1.032	1.003	1.290	1.777	0.754	1.330	1.309	1.405	1.250	0.000	2.237	1.223	1
SO_3	4.860	0.672	12.293	6.270	2.528	10.342	2.540	0.780	9.162	4.800	1.063	7.754	4.618	1
Cl	0.410	0.000	1.137	0.430	0.000	0.899	0.300	0.000	1.429	0.290	0.000	0.519	0.358	0
F	--	--	0.092	--	--	0.159	--	--	0.117	--	--	0.000	--	
H_2O	--	0.227	--	--	0.853	--	--	0.263	--	--	0.000	--	--	0
Proportion*	--	0.6496	0.3504	--	0.5322	0.4678	--	0.8034	0.1966	--	0.4421	0.5579	--	0.

*These proportions represent the maximum possible proportion of crystalline material (upper limit) and, consequently, the minimum proportion of amorphous material (lower limit). Bulk crystalline and amorphous component compositions computed with FULLPAT-estimated proportions are reported in Morris et al. (2016) and Rampe et al. (2017).

TABLE 12D. Stimson formation samples.

	Big Sky			Greenhorn			Lubango			Okoruso			Stimson Average		
	APXS	**Xtal†**	**Amorph**	**APXS**	**Xtal**	**Amorph**	**APXS**	**Xtal**	**Amorph**	**APXS**	**Xtal**	**Amorph**	**APXS**	**Xtal**	**Amorph**
SiO_2	42.950	46.360	24.133	53.240	34.126	63.525	59.800	39.102	68.000	45.130	45.546	43.909	50.280	41.284	49.892
TiO_2	1.000	0.000	6.587	1.000	0.000	1.537	1.120	0.000	1.572	0.940	0.000	3.654	1.015	0.000	3.338
Al_2O_3	11.520	13.572	0.123	3.920	11.234	0.000	3.090	10.636	0.000	9.640	11.723	3.620	7.043	11.791	0.936
Cr_2O_3	0.510	0.000	3.359	0.450	0.000	0.692	0.290	0.000	0.407	0.410	0.000	1.594	0.415	0.000	1.513
FeO_T	21.550	22.299	17.478	15.250	24.763	10.159	8.220	16.543	4.792	22.400	24.381	16.668	16.855	21.997	12.274
MnO	0.401	0.000	2.641	0.137	0.000	0.211	0.090	0.000	0.126	0.390	0.000	1.516	0.255	0.000	1.124
MgO	7.490	6.210	14.676	1.810	2.461	1.462	1.550	3.192	0.874	8.970	7.040	14.539	4.955	4.726	7.888
CaO	6.120	7.222	0.000	7.800	12.155	5.470	8.230	12.350	6.516	6.370	5.824	7.943	7.130	9.388	4.982
Na_2O	3.080	2.554	6.030	2.430	3.093	2.076	1.920	3.694	1.189	3.080	3.026	3.235	2.628	3.092	3.133
K_2O	0.460	0.292	1.402	0.300	0.000	0.461	0.310	0.000	0.435	0.370	0.498	0.000	0.360	0.198	0.575
P_2O_5	0.720	0.548	1.686	1.150	0.000	1.767	1.330	0.000	1.867	0.750	0.675	0.966	0.988	0.306	1.572
SO_3	3.350	0.894	17.076	11.920	11.908	11.934	13.710	13.419	13.773	0.960	1.149	0.412	7.485	6.843	10.799
Cl	0.730	0.000	4.809	0.460	0.000	0.707	0.320	0.000	0.449	0.500	0.000	1.944	0.503	0.000	1.977
F	--	--	0.049	--	--	0.000	--	--	0.000	--	--	0.060	--	--	0.055
H_2O	--	0.000	--	--	0.259	--	--	1.064	--	--	0.077	--	--	0.467	--
Prop.*	--	0.85897	0.14103	--	0.35592	0.64408	--	0.2939	0.7061	--	0.7542	0.2458		0.5657	0.4343

†Raw Big Sky crystalline abundances (Yen et al. 2017) were used for the amorphous calculations rather than the contamination-subtracted abundances reported in Table 2.
*These proportions represent the maximum possible proportion of crystalline material (upper limit) and, consequently, the minimum proportion of amorphous material (lower limit). Bulk crystalline and amorphous component compositions computed with FULLPAT-estimated proportions are reported in Yen et al. (2017).

This is a preprint, the final version is subject to change, of the American Mineralogist (MSA)
Cite as Authors (Year) Title. American Mineralogist, in press.
DOI: http://dx.doi.org/10.2138/am-2018-6124

TABLE 12E. Stimson formation samples

	Unaltered Stimson Average			Altered Stimson Average		
	APXS	**Xtal**	**Amorph**	**APXS**	**Xtal**	**Amorph**
SiO_2	44.040	45.953	34.021	56.520	36.614	65.763
TiO_2	0.970	0.000	5.121	1.060	0.000	1.555
Al_2O_3	10.580	12.648	1.872	3.505	10.935	0.000
Cr_2O_3	0.460	0.000	2.477	0.370	0.000	0.550
FeO_T	21.975	23.340	17.073	11.735	20.653	7.476
MnO	0.396	0.000	2.079	0.114	0.000	0.169
MgO	8.230	6.625	14.608	1.680	2.827	1.168
CaO	6.245	6.523	3.972	8.015	12.253	5.993
Na_2O	3.080	2.790	4.633	2.175	3.394	1.633
K_2O	0.415	0.395	0.701	0.305	0.000	0.448
P_2O_5	0.735	0.612	1.326	1.240	0.000	1.817
SO_3	2.155	1.022	8.744	12.815	12.664	12.854
Cl	0.615	0.000	3.377	0.390	0.000	0.578
F	--	--	0.055	--	--	0.000
H_2O	--	0.039	--	--	0.662	--
Prop*.	--	0.807	0.193	--	0.325	0.675

*These proportions represent the maximum possible proportion of crystalline material (upper limit) and, consequently, the minimum proportion of amorphous material (lower limit). Bulk crystalline and amorphous component compositions computed with FULLPAT-estimated proportions are reported in Yen et al. (2017).

This is a preprint, the final version is subject to change, of the American Mineralogist (MSA)
Cite as Authors (Year) Title. American Mineralogist, in press.
DOI: http://dx.doi.org/10.2138/am-2018-6124

FIGURES

Figure 1. CheMin sample wheel incorporates twenty-seven reusable sample cells and five calibration standards.

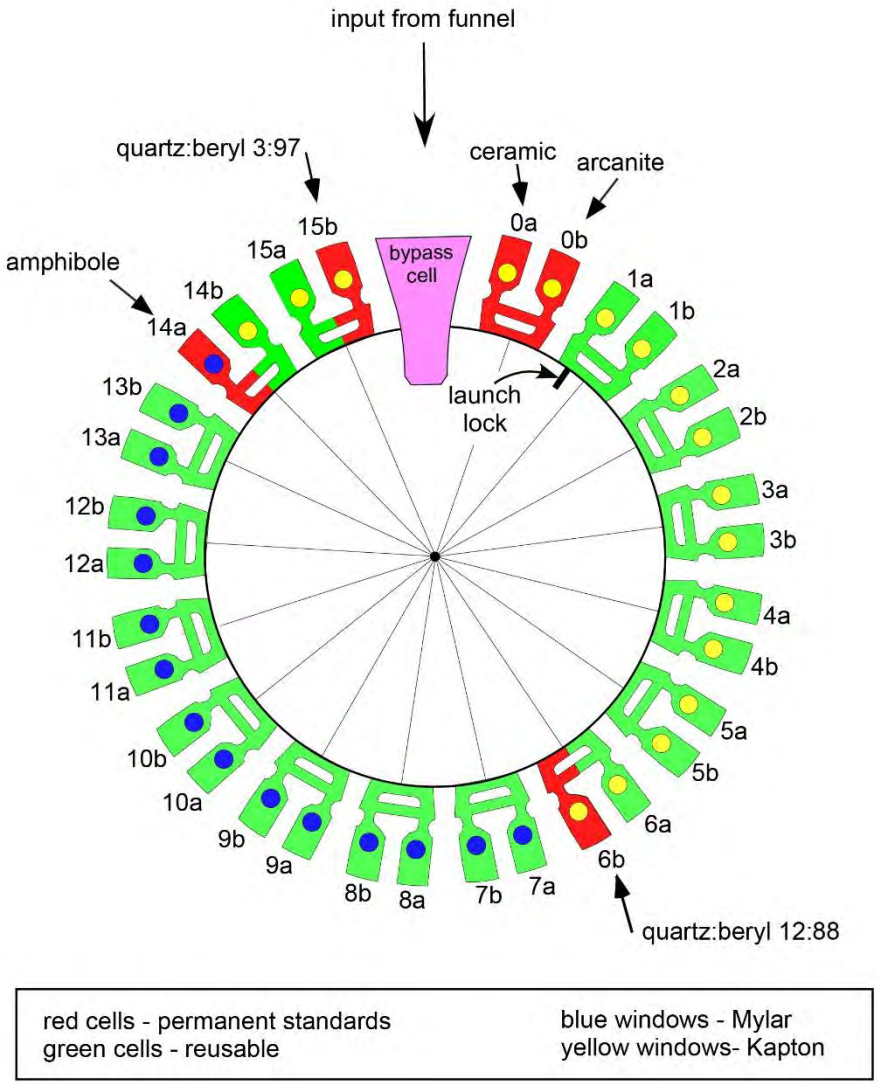

This is a preprint, the final version is subject to change, of the American Mineralogist (MSA)
Cite as Authors (Year) Title. American Mineralogist, in press.
DOI: http://dx.doi.org/10.2138/am-2018-6124

Figure 2. CheMin sample cell. The incident X-ray beam passes from the X-ray source, through the sample cell, and interacts with the sample material, causing X-rays to diffract and strike the CCD. The angle between the transmitted beam and the diffracted beam is 2θ.

A displacement of the sample cell, resulting in an increase or decrease in sample cell-to-CCD distance, will result in an error in 2θ measurement. The angle 2θ between the transmitted and diffracted X-ray beams is invariant; however, the position of the diffracted beam on the CCD is moved laterally, resulting in an inaccurate apparent 2θ.

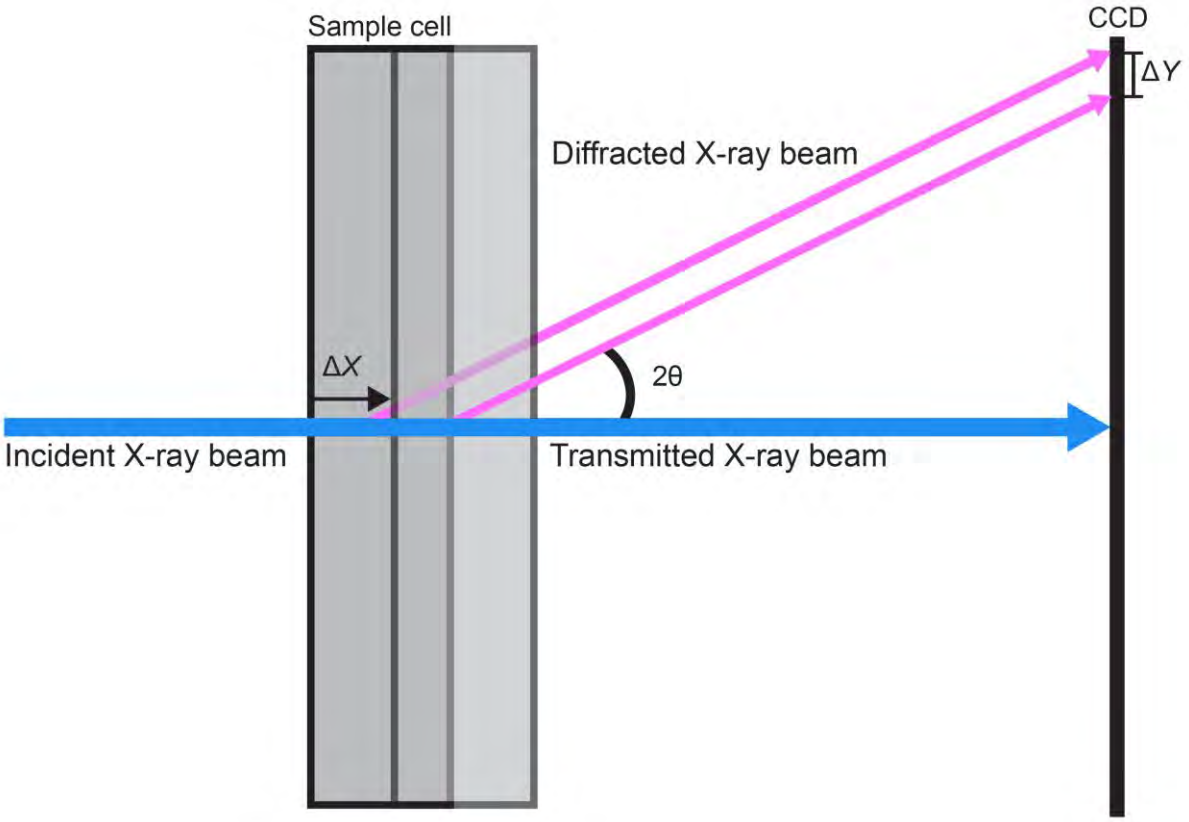

This is a preprint, the final version is subject to change, of the American Mineralogist (MSA)
Cite as Authors (Year) Title. American Mineralogist, in press.
DOI: http://dx.doi.org/10.2138/am-2018-6124

FIGURE 3a. Plagioclase *c* vs γ unit-cell parameters. Black circles represent literature plagioclase values. The red square represents pre-calibration CheMin Rocknest plagioclase values.

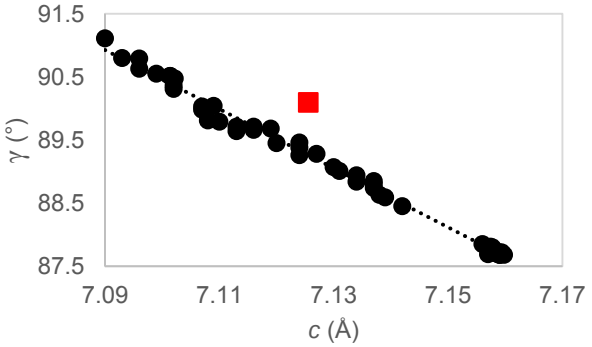

FIGURE 3b. Plagioclase *c* vs γ unit-cell parameters - sample cell offset calibration. Black circles represent plagioclase data from the literature. Red squares represent refined plagioclase unit-cell parameters from the Rocknest sample with variations in sample cell-to-CCD distances from -45 µm to 45 µm.

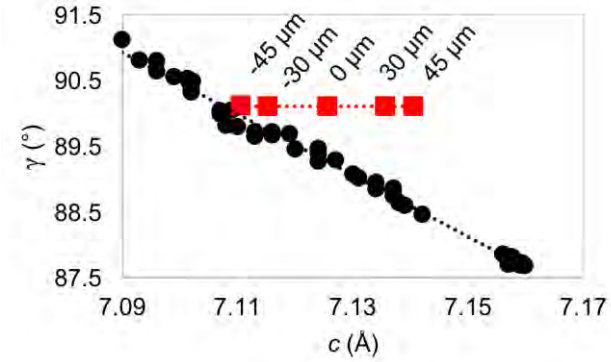

FIGURE 3c. Plagioclase *c* vs γ unit-cell parameters. Black circles represent literature plagioclase values. Red square represents CheMin Rocknest plagioclase values calibrated with a sample cell offset distance of -53 µm.

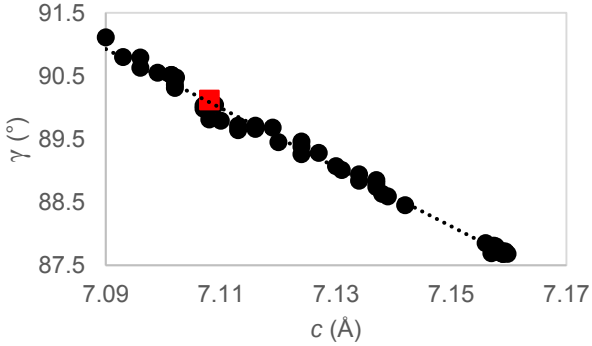

This is a preprint, the final version is subject to change, of the American Mineralogist (MSA)
Cite as Authors (Year) Title. American Mineralogist, in press.
DOI: http://dx.doi.org/10.2138/am-2018-6124

FIGURE 4a-f. Olivine unit-cell parameter trends. Black circles represent literature data. Red diamonds represent the pre-calibration CheMin Rocknest data. Blue squares represent the sample cell offset calibrated CheMin Rocknest data. These figures show that, despite the calibration being based solely on plagioclase, its effects produced internally consistent unit-cell parameters for the other phases.

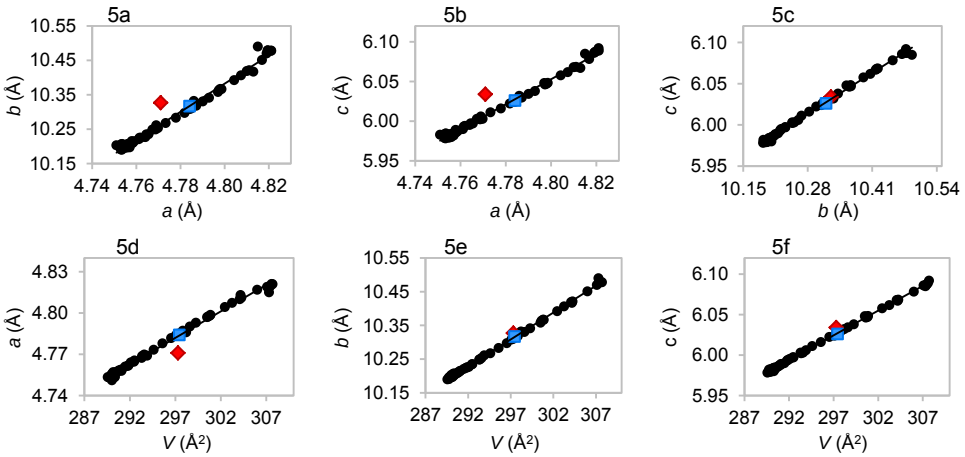

This is a preprint, the final version is subject to change, of the American Mineralogist (MSA)
Cite as Authors (Year) Title. American Mineralogist, in press.
DOI: http://dx.doi.org/10.2138/am-2018-6124

FIGURE 5. Comparison of martian meteorite plagioclase compositional distribution (blue bars) (Papike et al. 2009; Santos et al. 2015; Wittmann et al. 2015; Nyquist et al. 2016; Hewins et al. 2017) with the range of composition of plagioclase measured with CheMin (red overlay). Windjana is excluded from the range because of its extremely high uncertainty.

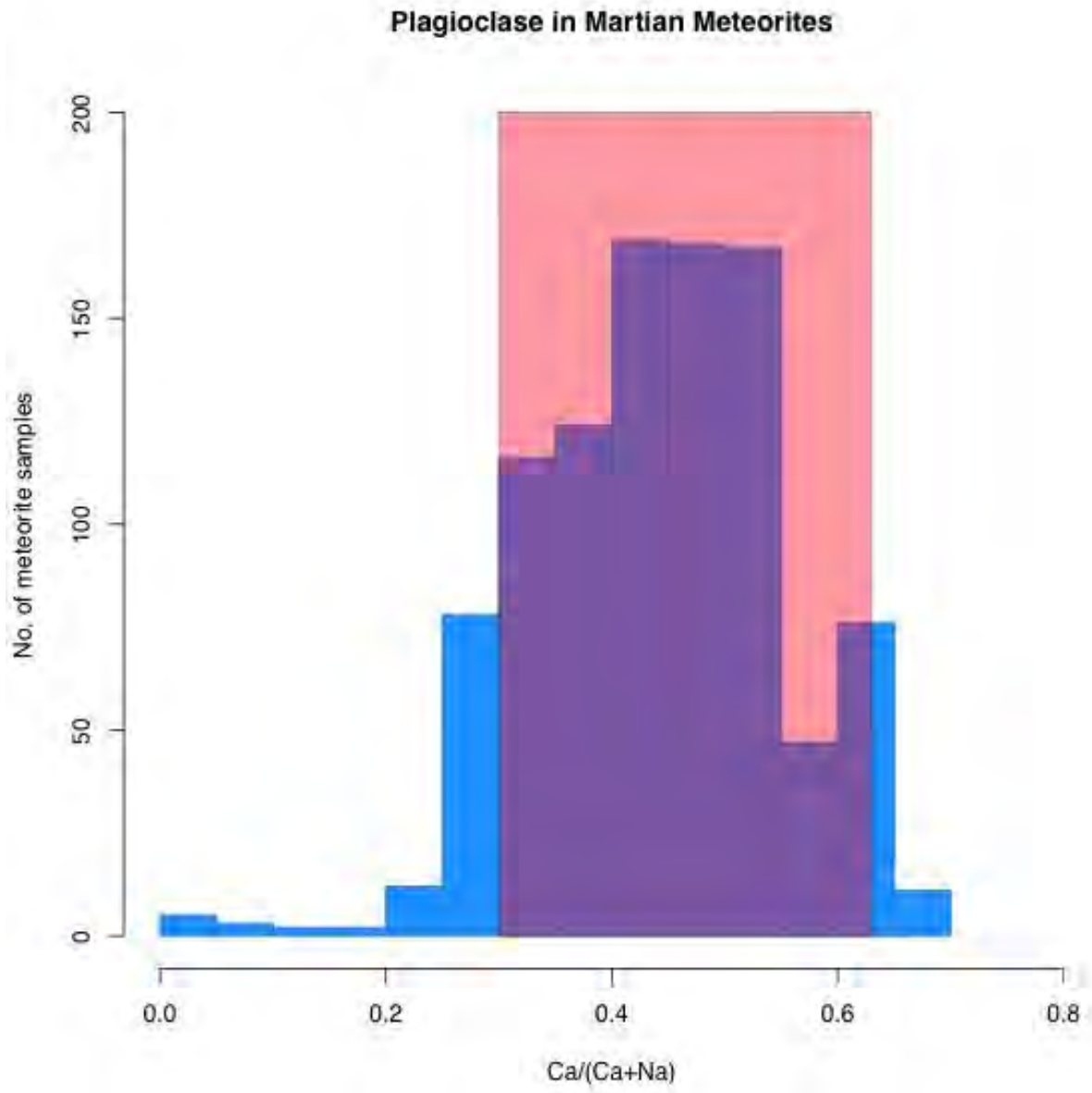

This is a preprint, the final version is subject to change, of the American Mineralogist (MSA)
Cite as Authors (Year) Title. American Mineralogist, in press.
DOI: http://dx.doi.org/10.2138/am-2018-6124

FIGURE 6. Alkali feldspar quadrilateral: composition and Al-Si ordering as a function of *c* and *b* unit-cell parameters. Black circles represent literature end-members. Red squares represent CheMin analyzed Gale crater samples with 1σ error bars: JK = John Klein, CB = Cumberland, WJ = Windjana, CH = Confidence Hills, TP = Telegraph Peak, BK = Buckskin. Composition trends from $NaAlSi_3O_8$ at the low albite – high albite edge to $KAlSi_3O_8$ at the low microcline – high sanidine edge. Al-Si ordering trends from completely ordered at the low albite – low microcline edge to completely disordered at the high albite – high sanidine edge.

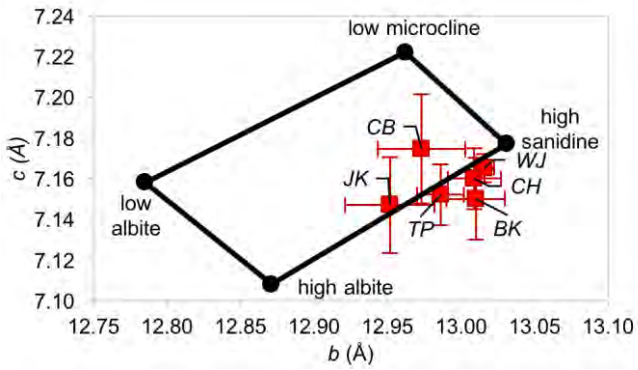

Figure 7. Comparison of martian meteorite pyroxene compositional distribution (gray circles) (Papike et al. 2009, Santos et al. 2015; Wittmann et al. 2015; Nyquist et al. 2016; Hewins et al. 2017) with that of the compositions observed in Gale crater pyroxene. Gale crater augite is represented as triangles, pigeonite as squares, and orthopyroxene as circles. Error ellipses are at 1σ. Red = Rocknest; dark red = Gobabeb; orange = John Klein; dark orange = Cumberland; black = Windjana; light purple = Confidence Hills; medium purple = Mojave2; dark purple = Telegraph Peak; light green = Big Sky; dark blue = Greenhorn; light blue = Lubango; dark green = Okoruso.

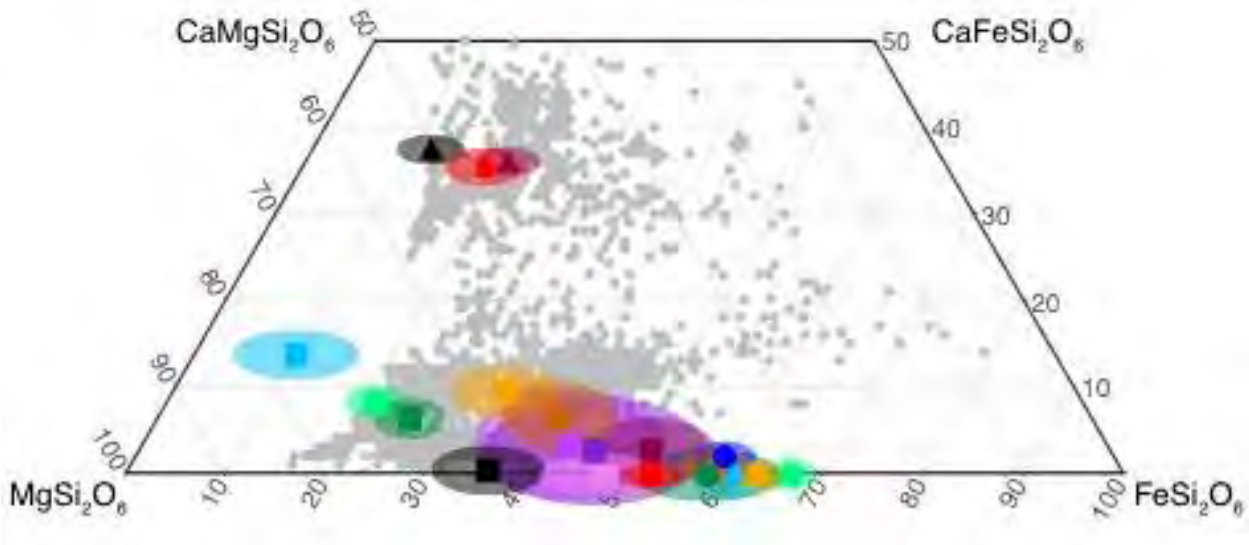

This is a preprint, the final version is subject to change, of the American Mineralogist (MSA)
Cite as Authors (Year) Title. American Mineralogist, in press.
DOI: http://dx.doi.org/10.2138/am-2018-6124

FIGURE 8. Comparison of martian meteorite Fe-Mg olivine compositional distribution (blue bars) (Papike et al. 2009; Hewins et al. 2017) with the range of composition observed in Gale crater olivine (red overlay).

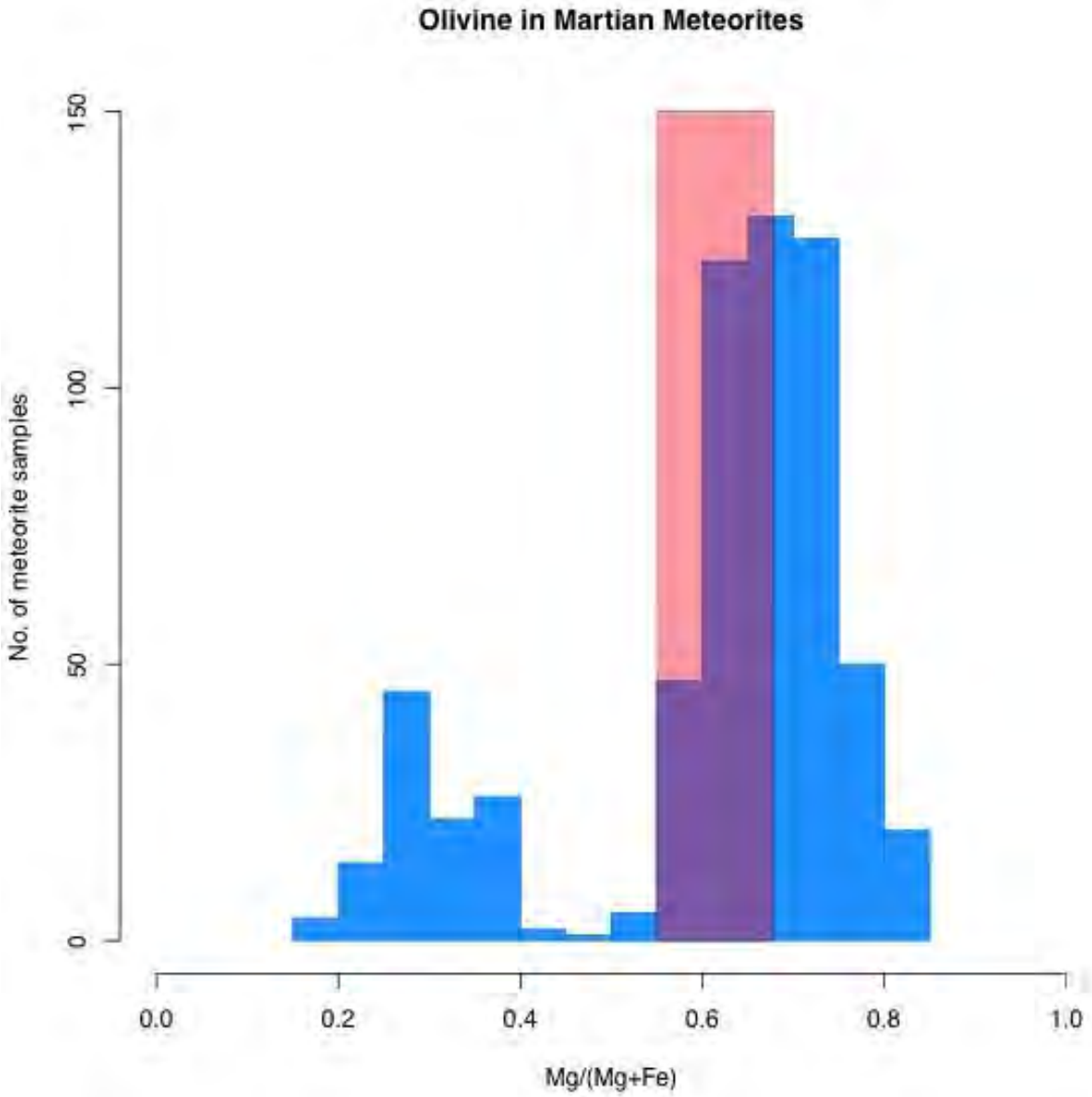

This is a preprint, the final version is subject to change, of the American Mineralogist (MSA)
Cite as Authors (Year) Title. American Mineralogist, in press.
DOI: http://dx.doi.org/10.2138/am-2018-6124

FIGURE 9. Select spinel oxide phases (M_3O_4) as a function of Fe content and *a* unit-cell parameter. The blue region represents the range of Gale crater magnetite.

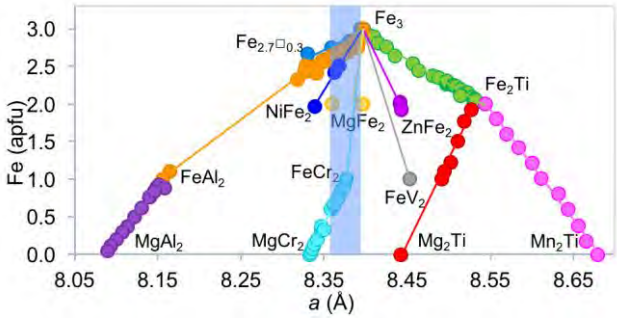

FIGURE 10. Alunite-jarosite group minerals as a function of the *a* and *c* unit-cell parameters. The CheMin Mojave2 sample unit-cell parameters are represented by the red square and correspond to a composition of $(K_{0.51(12)}Na_{0.49})(Fe_{0.89(2)}Al_{0.11})(SO_4)_2(OH)_6$. jrs = jarosite, alu = alunite, njrs = natrojarosite, nalu = natroalunite, ajrs = ammoniojarosite, aalu = ammonioalunite, hjrs = hydroniumjarosite.

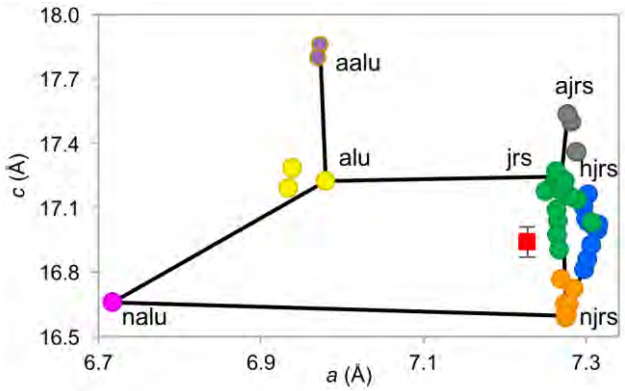

This is a preprint, the final version is subject to change, of the American Mineralogist (MSA)
Cite as Authors (Year) Title. American Mineralogist, in press.
DOI: http://dx.doi.org/10.2138/am-2018-6124

Figure 11a. Pyroxene quadrilateral (Lindsley 1983) plotted with augite, pigeonite, and olivine chemical composition from CheMin wind-blown soils, Rocknest and Gobabeb. Augite is represented as triangles, pigeonite as squares, and olivine as hexagons. Error ellipses are at 1σ. Red = Rocknest and dark red = Gobabeb. Olivine compositions are plotted below the enstatite-ferrosilite join at the appropriate Fe/Mg ratios. The straight lines are joins between equilibrium pyroxene compositions, and include the equilibrium Fe-Mg partitioning between the various pyroxenes. Contour represent temperature of formation at 100°C intervals.

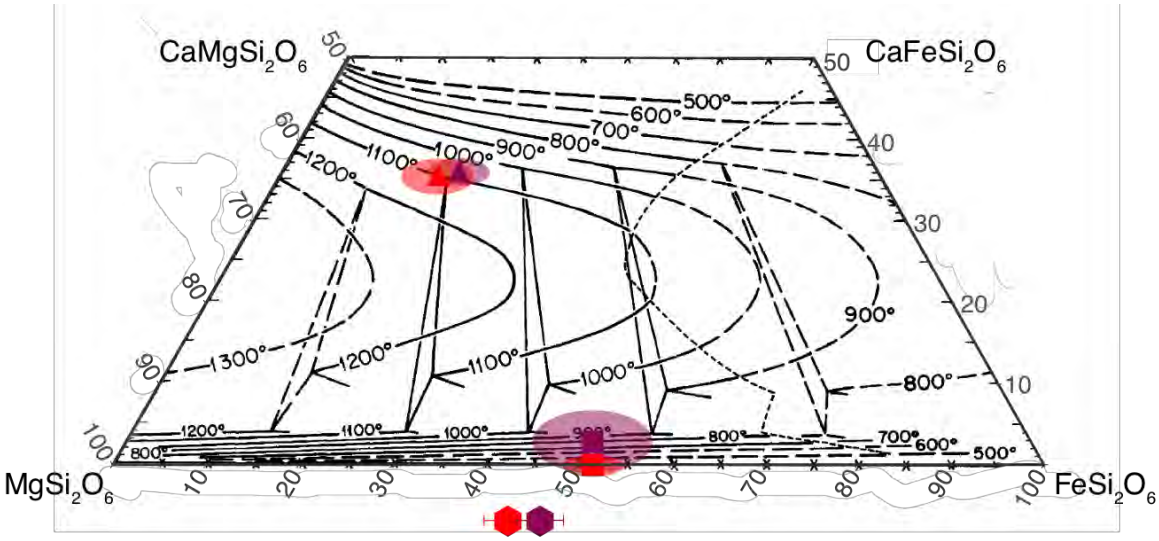

Figure 11b. Pyroxene quadrilateral (Lindsley 1983) plotted with augite, pigeonite, and olivine chemical composition from CheMin analyzed samples of Yellowknife Bay, John Klein and Cumberland, as well as the Windjana sandstone. Augite is represented as triangles, pigeonite as squares, and olivine as hexagons. Error ellipses are at 1σ. orange = John Klein, dark orange = Cumberland, and black = Windjana. Olivine compositions are plotted below the enstatite-ferrosilite join at the appropriate Fe/Mg ratios. The straight lines are joins between equilibrium pyroxene compositions, and include the equilibrium Fe-Mg partitioning between the various pyroxenes. Contour represent temperature of formation at 100°C intervals.

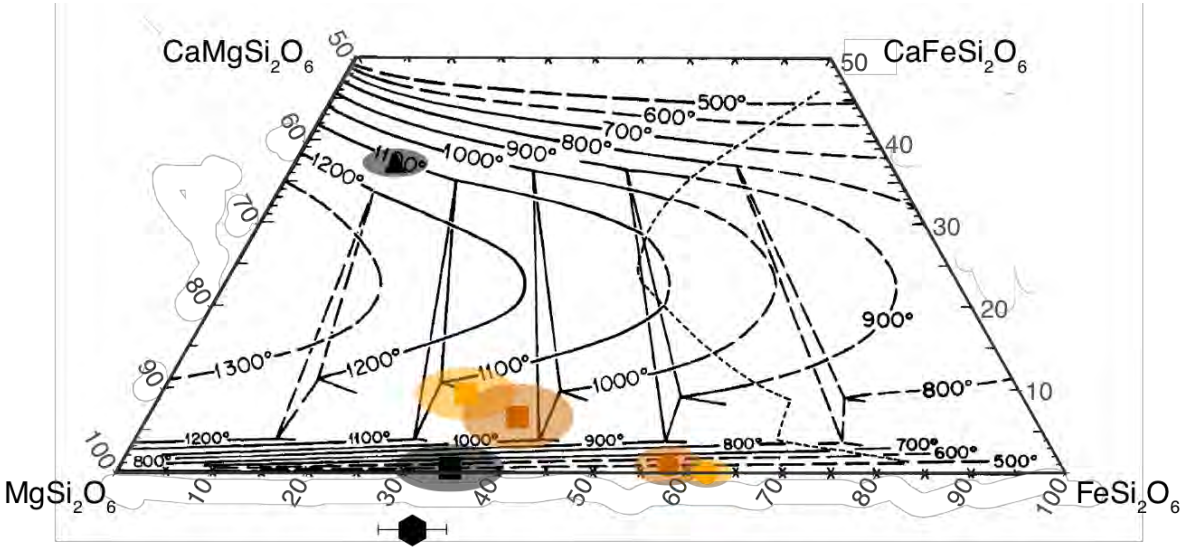

This is a preprint, the final version is subject to change, of the American Mineralogist (MSA)
Cite as Authors (Year) Title. American Mineralogist, in press.
DOI: http://dx.doi.org/10.2138/am-2018-6124

Figure 11c. Pyroxene quadrilateral (Lindsley 1983) plotted with pigeonite and orthopyroxene chemical composition from CheMin analyzed samples of the Murray formation (Confidence Hills, Mojave2, and Telegraph Peak in shades of purple) and the Stimson formation (unaltered Big Sky and Okoruso in shades of green; altered Greenhorn and Lubango in shades of blue). Pigeonite is represented as squares and orthopyroxene as circles. Error ellipses are at 1σ. Light purple = Confidence Hills, medium purple = Mojave2, dark purple = Telegraph Peak, light green = Big Sky, dark blue = Greenhorn, light blue = Lubango, and dark green = Okoruso. The straight lines are joins between equilibrium pyroxene compositions, and include the equilibrium Fe-Mg partitioning between the various pyroxenes. Contour represent temperature of formation at 100°C intervals.

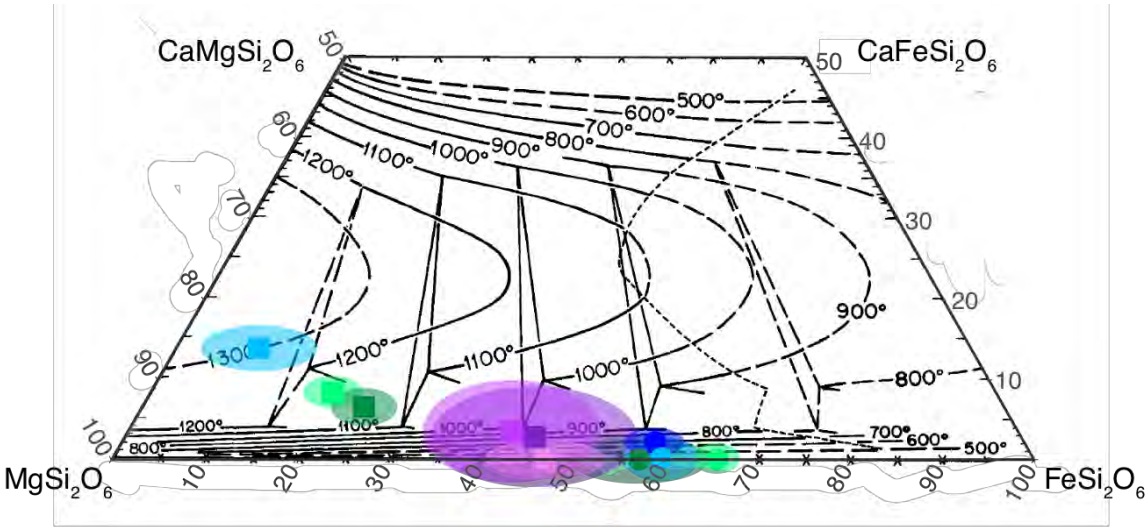

Figure 12. Comparison of the minimum possible proportion of amorphous material calculated by mass balance from measured composition (this study) versus an estimate of the amorphous-component proportion by full pattern fitting (FULLPAT) of the diffracted intensities of the amorphous material.

This is a preprint, the final version is subject to change, of the American Mineralogist (MSA)
Cite as Authors (Year) Title. American Mineralogist, in press.
DOI: http://dx.doi.org/10.2138/am-2018-6124

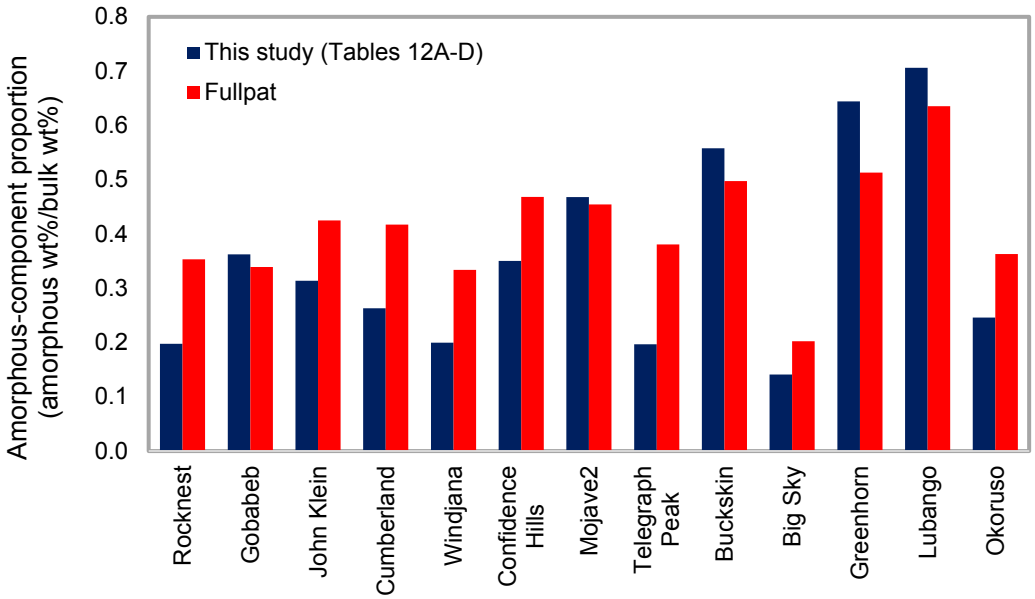

Appendices

Appendix 1 – Sample cell offset calibration data

Table A1a. Plagioclase regression data

Plagioclase-phase								
Chemical composition	*a* (Å)	*b* (Å)	*c* (Å)	α (°)	β (°)	γ (°)	*V* (Å^3)	Reference
$Na_{0.991}Ca_{0.007}K_{0.002}Al_{1.007}Si_{2.993}O_8$	8.139	12.782	7.157	94.29	116.6	87.69	663.869	[2]
$Na_{0.977}Ca_{0.017}K_{0.006}Al_{1.017}Si_{2.983}O_8$	8.139	12.785	7.158	94.2	116.61	87.76	664.139	[2]
$Na_{0.997}K_{0.003}Al_{1.000}Si_{3.000}O_8$	8.141	12.786	7.159	94.25	116.59	87.69	664.516	[2]
$Na_{0.983}Ca_{0.005}K_{0.012}Al_{1.005}Si_{2.995}O_8$	8.141	12.785	7.159	94.26	116.59	87.69	664.456	[2]
$Na_{0.875}Ca_{0.111}K_{0.014}Al_{1.111}Si_{2.889}O_8$	8.148	12.798	7.156	94.2	116.57	87.85	665.604	[2]
$Na_{0.865}Ca_{0.130}K_{0.005}Al_{1.130}Si_{2.870}O_8$	8.149	12.804	7.142	94.07	116.52	88.45	665.094	[2]
$Na_{0.828}Ca_{0.165}K_{0.007}Al_{1.165}Si_{2.835}O_8$	8.151	12.814	7.138	94.01	116.5	88.63	665.556	[2]
$Na_{0.815}Ca_{0.176}K_{0.009}Al_{1.176}Si_{2.824}O_8$	8.153	12.824	7.134	93.95	116.46	88.84	666.122	[2]
$Na_{0.773}Ca_{0.215}K_{0.012}Al_{1.215}Si_{2.785}O_8$	8.153	12.83	7.134	93.9	116.43	88.94	666.635	[2]
$Na_{0.822}Ca_{0.172}K_{0.006}Al_{1.172}Si_{2.828}O_8$	8.154	12.826	7.137	93.94	116.48	88.74	666.494	[2]
$Na_{0.758}Ca_{0.239}K_{0.003}Al_{1.239}Si_{2.761}O_8$	8.154	12.847	7.12	93.79	116.42	89.45	666.328	[2]
$Na_{0.816}Ca_{0.179}K_{0.005}Al_{1.179}Si_{2.821}O_8$	8.155	12.834	7.13	93.88	116.45	89.07	666.509	[2]
$Na_{0.806}Ca_{0.185}K_{0.009}Al_{1.185}Si_{2.815}O_8$	8.158	12.831	7.137	93.94	116.45	88.8	667.247	[2]
$Na_{0.734}Ca_{0.256}K_{0.010}Al_{1.256}Si_{2.744}O_8$	8.158	12.837	7.124	93.8	116.4	89.26	666.667	[2]
$Na_{0.737}Ca_{0.253}K_{0.010}Al_{1.253}Si_{2.747}O_8$	8.159	12.843	7.127	93.8	116.41	89.28	667.279	[2]
$Na_{0.781}Ca_{0.210}K_{0.009}Al_{1.210}Si_{2.790}O_8$	8.161	12.836	7.131	93.89	116.45	89.01	667.2	[2]
$Na_{0.643}Ca_{0.353}K_{0.004}Al_{1.353}Si_{2.647}O_8$	8.161	12.859	7.116	93.66	116.3	89.71	667.878	[2]
$Na_{0.759}Ca_{0.202}K_{0.039}Al_{1.202}Si_{2.798}O_8$	8.162	12.827	7.137	93.88	116.46	88.85	667.353	[2]

This is a preprint, the final version is subject to change, of the American Mineralogist (MSA)
Cite as Authors (Year) Title. American Mineralogist, in press.
DOI: http://dx.doi.org/10.2138/am-2018-6124

$Na_{0.712}Ca_{0.280}K_{0.008}Al_{1.280}Si_{2.720}O_8$	8.163	12.853	7.124	93.71	116.36	89.38	668.188	[2]
$Na_{0.520}Ca_{0.478}K_{0.002}Al_{1.478}Si_{2.522}O_8$	8.166	12.851	7.113	93.61	116.26	89.64	667.888	[2]
$Na_{0.564}Ca_{0.432}K_{0.004}Al_{1.432}Si_{2.568}O_8$	8.167	12.856	7.113	93.6	116.27	89.71	668.158	[2]
$Na_{0.455}Ca_{0.537}K_{0.008}Al_{1.537}Si_{2.463}O_8$	8.169	12.862	7.108	93.58	116.22	89.81	668.436	[2]
$Na_{0.584}Ca_{0.374}K_{0.042}Al_{1.374}Si_{2.626}O_8$	8.171	12.862	7.119	93.59	116.3	89.68	669.206	[2]
$Na_{0.550}Ca_{0.437}K_{0.013}Al_{1.437}Si_{2.563}O_8$	8.172	12.865	7.116	93.6	116.27	89.66	669.334	[2]
$Na_{0.447}Ca_{0.543}K_{0.010}Al_{1.543}Si_{2.457}O_8$	8.172	12.861	7.107	93.52	116.22	90.03	668.506	[2]
$Na_{0.452}Ca_{0.538}K_{0.010}Al_{1.538}Si_{2.462}O_8$	8.173	12.855	7.11	93.58	116.23	89.79	668.537	[2]
$Na_{0.400}Ca_{0.598}K_{0.002}Al_{1.598}Si_{2.402}O_8$	8.173	12.862	7.107	93.56	116.19	89.98	668.797	[2]
$Na_{0.311}Ca_{0.687}K_{0.002}Al_{1.687}Si_{2.313}O_8$	8.175	12.865	7.102	93.5	116.14	90.31	668.846	[2]
$Na_{0.303}Ca_{0.690}K_{0.007}Al_{1.690}Si_{2.310}O_8$	8.179	12.869	7.102	93.49	116.16	90.36	669.251	[2]
$Na_{0.198}Ca_{0.800}K_{0.002}Al_{1.800}Si_{2.200}O_8$	8.179	12.868	7.093	93.34	116.08	90.8	668.719	[2]
$Na_{0.069}Ca_{0.931}Al_{1.931}Si_{2.069}O_8$	8.179	12.873	7.09	93.21	115.97	91.11	669.261	[2]
$Na_{0.407}Ca_{0.581}K_{0.012}Al_{1.581}Si_{2.419}O_8$	8.18	12.87	7.109	93.52	116.2	90.04	669.928	[2]
$Na_{0.227}Ca_{0.770}K_{0.003}Al_{1.770}Si_{2.230}O_8$	8.18	12.869	7.096	93.38	116.13	90.63	668.905	[2]
$Na_{0.263}Ca_{0.731}K_{0.006}Al_{1.731}Si_{2.269}O_8$	8.181	12.87	7.099	93.41	116.1	90.55	669.509	[2]
$Na_{0.181}Ca_{0.819}Al_{1.819}Si_{2.181}O_8$	8.181	12.871	7.096	93.34	116.1	90.79	669.212	[2]
$Ca_{0.65}Na_{0.32}Si_{2.38}Al_{1.62}O_8$	8.1736	12.874	7.1022	93.46	116.05	90.48	669.65	[9]
$Ca_{0.634}Na_{0.366}Si_{2.348}Al_{1.648}O_8$	8.1747	12.871	7.1014	93.46	116.09	90.51	669.3	[9]
$Ca_{0.650}Na_{0.350}Si_{2.348}Al_{1.648}O_8$	8.1747	12.871	7.1014	93.46	116.09	90.51	669.3	[9]
$Na_{0.986}Al_{1.005}Si_{2.995}O_8$	8.142	12.785	7.159	94.19	116.61	87.68	664.48	[5]
$NaAl_{1.004}Si_{2.994}O_8$	8.142	12.785	7.159	94.19	116.61	87.68	664.48	[5]
$NaAlSi_3O_8$	8.137	12.785	7.1583	94.26	116.6	87.71	664.01	[1]
$NaAlSi_3O_8$	8.1372	12.787	7.1574	94.25	116.61	87.81	664.04	[3]
$NaAlSi_3O_8$	8.133	12.773	7.159	94.23	116.64	87.72	662.92	[6]
$Na_{0.98}Ca_{0.02}Si_{2.98}Al_{1.02}O_8$	8.1459	12.797	7.1578	94.25	116.6	87.8	665.34	[4]
$Na_{0.99}Ca_{0.01}Al_{1.03}Si_{2.97}O_8$	8.135	12.784	7.1594	94.27	116.59	87.72	663.92	[8]
$Na_{0.99}Ca_{0.01}Al_{1.03}Si_{2.97}O_8$	8.1365	12.788	7.1584	94.23	116.58	87.7	664.26	[8]
$NaAlSi_3O_8$	8.1409	12.789	7.1598	94.27	116.59	87.68	664.73	[8]
$Na_{0.821}Ca_{0.179}Al_{1.179}Si_{2.821}O_8$	8.154	12.823	7.139	94.06	116.5	88.59	666.32	[7]
$Na_{0.723}Ca_{0.277}Al_{1.277}Si_{2.723}O_8$	8.169	12.851	7.124	93.63	116.4	89.46	668.39	[7]

[1] Armbruster, T., Burgi, H.B., Kunz, M., Gnos, E., Bronnimann, S., and Lienert, C. (1990) Variation of displacement parameters in structure refinements of low albite. American Mineralogist, 75, 135–140.

[2] Bambauer, H.U., Corlett, M., Eberhard, E., and Viswanathan, K. (1967) Diagrams for the determination of plagioclases using X-ray powder methods (Part III of laboratory investigations of plagioclases). Schweizerische Mineralogische und Petrographische Mitteilungen, 47, 333-349.

[3] Downs, R.T., Hazen, R.M., and Finger, L.W. (1994) The high-pressure crystal chemistry of low albite and the origin of the pressure dependency of Al-Si ordering. American Mineralogist, 79, 1042–1052.

This is a preprint, the final version is subject to change, of the American Mineralogist (MSA)
Cite as Authors (Year) Title. American Mineralogist, in press.
DOI: http://dx.doi.org/10.2138/am-2018-6124

[4] Gualtieri, A.F. (2000) Accuracy of XRPD QPA using the combined Rietveld-RIR method. Journal of Applied Crystallography, 33, 267-278.
[5] Harlow, G., and Brown Jr, G.E. (1980) Low Albite- an X-Ray and Neutron Diffraction Study. American Mineralogist, 65, 986–995.
[6] Meneghinello, E., Alberti, A., and Cruciani, G. (1999) Order-disorder process in the tetrahedral sites of albite. American Mineralogist, 84, 1144–1151.
[7] Phillips, M.W., Colville, A.A., and Ribbe, P.H. (1971) The crystal structures of two oligoclases: A comparison with low and high albite. Zeitschrift fur Kristallographie, 133, 43–65.
[8] RRUFF.info
[9] Wenk, H., Joswig, W., Tagai, T., Korekawa, M., and Smith, B.K. (1980) The average structure of An 62-66 labradorite. American Mineralogist, 65, 81–95.

This is a preprint, the final version is subject to change, of the American Mineralogist (MSA)
Cite as Authors (Year) Title. American Mineralogist, in press.
DOI: http://dx.doi.org/10.2138/am-2018-6124

1143 Table A1b. Olivine regression data

	Olivine-phase				
Chemical composition	*a* (Å)	*b* (Å)	*c* (Å)	*V* (Å^3)	Reference
Mg_2SiO_4	4.7534	10.1902	5.9783	289.577	[9]
Mg_2SiO_4	4.753	10.191	5.982	289.755	[7]
Mg_2SiO_4	4.753	10.196	5.979	289.76	[6]
Mg_2SiO_4	4.754	10.1971	5.9806	289.92	[21]
Mg_2SiO_4	4.7549	10.1985	5.9792	289.948	[4]
Mg_2SiO_4	4.755	10.196	5.9809	289.97	[24]
Mg_2SiO_4	4.7534	10.1989	5.9813	289.97	[13]
Mg_2SiO_4	4.751	10.203	5.983	290.023	[23]
Mg_2SiO_4	4.7558	10.1965	5.9817	290.068	[20]
Mg_2SiO_4	4.7545	10.2	5.9814	290.08	[14]
Mg_2SiO_4	4.7553	10.1977	5.982	290.09	[15]
Mg_2SiO_4	4.757	10.197	5.982	290.17	[24]
Mg_2SiO_4	4.75534	10.20141	5.98348	290.266	[25]
Mg_2SiO_4	4.756	10.207	5.98	290.296	[22]
Mg_2SiO_4	4.7533	10.2063	5.9841	290.31	[5]
Mg_2SiO_4	4.7536	10.2066	5.9845	290.36	[18]
$Mg_{1.997}Si_{0.995}O_4$	4.7552	10.1985	5.9822	290.112	[12]
$Mg_{1.98}Fe_{0.02}SiO_4$	4.7555	10.1999	5.9816	290.14	[21]
$Mg_{1.96}Fe_{0.04}SiO_4$	4.7563	10.2026	5.9842	290.39	[21]
$Mg_{1.94}Fe_{0.06}SiO_4$	4.7571	10.2053	5.9831	290.47	[21]
$Mg_{1.92}Fe_{0.08}SiO_4$	4.7578	10.2085	5.9857	290.72	[21]
$Mg_{1.91}Fe_{0.09}SiO_4$	4.7584	10.2099	5.9863	290.83	[21]
$Mg_{1.9}Fe_{0.1}SiO_4$	4.758	10.2115	5.9865	290.86	[21]
$Mg_{1.88}Fe_{0.12}SiO_4$	4.759	10.2145	5.988	291.08	[21]
$Mg_{1.84}Fe_{0.16}SiO_4$	4.7579	10.2151	5.989	291.08	[17]
$Mg_{1.82}Fe_{0.18}SiO_4$	4.7611	10.2207	5.99	291.49	[1]
$Mg_{1.82}Fe_{0.18}Si_1O_4$	4.7615	10.2248	5.9932	291.781	[20]
$Fe_{0.19}Mg_{1.81}SiO_4$	4.7641	10.2269	5.9952	292.098	[16]
$Mg_{1.8}Fe_{0.2}SiO_4$	4.762	10.225	5.994	291.857	[3]
$Mg_{1.77}Fe_{0.23}SiO_4$	4.7645	10.23467	5.99727	292.45	[11]
$Mg_{1.73}Fe_{0.27}SiO_4$	4.7655	10.2351	5.997	292.5	[21]
$Mg_{1.67}Fe_{0.33}SiO_4$	4.7673	10.2488	6.003	293.301	[20]
$Mg_{1.63}Fe_{0.37}SiO_4$	4.7687	10.2491	6.0023	293.36	[21]
$Mg_{1.6}Fe_{0.4}SiO_4$	4.7698	10.2531	6.003	293.58	[21]
$Mg_{1.6}Fe_{0.4}SiO_4$	4.769	10.261	6.006	293.9	[6]
$Mg_{1.55}Fe_{0.45}SiO_4$	4.7733	10.2676	6.0112	294.611	[10]
$Mg_{1.4}Fe_{0.6}SiO_4$	4.7779	10.2831	6.0161	295.58	[21]
$Mg_{1.3}Fe_{0.7}SiO_4$	4.7818	10.2972	6.0223	296.53	[21]
$Mg_{1.2}Fe_{0.8}SiO_4$	4.784	10.308	6.024	297.09	[6]
$Mg_{1.2}Fe_{0.8}SiO_4$	4.7849	10.3101	6.0263	297.29	[21]
$Mg_{1.15}Fe_{0.85}SiO_4$	4.7871	10.3181	6.0297	297.83	[21]

$Mg_{1.05}Fe_{0.95}SiO_4$	4.786	10.332	6.032	298.2	[19]
$Mg_{1.02}Fe_{0.98}SiO_4$	4.7901	10.3305	6.0343	298.6	[1]
$Fe_{1.0}Mg_{1.0}SiO_4$	4.7929	10.3412	6.038	299.27	[21]
$Fe_{1.18}Mg_{0.82}SiO_4$	4.7974	10.3635	6.0463	300.61	[21]
$Fe_{1.2}Mg_{0.8}SiO_4$	4.797	10.358	6.048	300.5	[6]
$Fe_{1.2}Mg_{0.8}SiO_4$	4.798	10.367	6.047	300.8	[6]
$Fe_{1.2}Mg_{0.8}SiO_4$	4.7986	10.3665	6.0482	300.87	[21]
$Fe_{1.4}Mg_{0.6}SiO_4$	4.8043	10.3923	6.0577	302.45	[21]
$Fe_{1.5}Mg_{0.5}SiO_4$	4.8074	10.4063	6.0618	303.25	[21]
$Fe_{1.6}Mg_{0.4}SiO_4$	4.81	10.419	6.068	304.08	[6]
$Fe_{1.6}Mg_{0.4}SiO_4$	4.813	10.417	6.067	304.18	[6]
$Fe_{1.6}Mg_{0.4}SiO_4$	4.8111	10.4213	6.0684	304.26	[21]
$Fe_{1.8}Mg_{0.2}SiO_4$	4.8169	10.4512	6.0783	306	[21]
Fe_2SiO_4	4.819	10.47	6.086	307.1	[6]
Fe_2SiO_4	4.815	10.49	6.085	307.3	[6]
Fe_2SiO_4	4.8195	10.4788	6.0873	307.42	[8]
Fe_2SiO_4	4.8195	10.4788	6.0873	307.424	[9]
Fe_2SiO_4	4.8211	10.4779	6.0889	307.58	[21]
Fe_2SiO_4	4.821	10.478	6.092	307.7	[2]

[1] Akamatsu, T., Kumazawa, M., Aikawa, N., and Takei, H. (1993) Pressure Effect on the Divalent Cation Distribution in Nonideal Solid Solution of Forsterite and Fayalite. Physics and Chemistry of Minerals, 19, 431-444.
[2] Annersten, H., Ericsson, T., and Filippidis, A. (1982) Cation ordering in Ni-Fe olivines. American Mineralogist, 67, 1212-1217.
[3] Birle, J.D., Gibbs, G.V., Moore, P.B., and Smith, J.V. (1968) Crystal structures of natural olivines. American Mineralogist, 53, 807-824.
[4] Bostrom, D. (1987) Single-crystal X-ray diffraction studies of synthetic Ni-Mg olivine solid solutions. American Mineralogist, 72, 965-972.
[5] Cernik, R.J., Murray, P.K., Pattison, P., and Fitch, A.N. (1990) A two-circle powder diffractometer for synchrotron radiation with a closed loop encoder feedback system. Journal of Applied Crystallography, 23, 292-296.
[6] Fisher G W, Medaris L G (1969) Cell dimensions and X-ray determinative curve for synthetic Mg-Fe olivines. American Mineralogist, 54, 741-753.
[7] Frances, C.A. (1985) New data on the forsterite-tephroite series. American Mineralogist, 70, 568-575.
[8] Fujino, K., Sasaki, S., Takeuchi, Y., and Sadanaga, R. (1981) X-ray determination of electron distributions in forsterite, fayalite and tephroite. Acta Crystallographica B, 37, 513-518.
[9] Fujino, K., Sasaki, S., Takeuchi, Y., and Sadanaga, R. (1981) X-ray determination of electron distributions in forsterite, fayalite and tephroite. Acta Crystallographica, B37, 513-518.
[10] Heinemann, R., Kroll, H., Kirfel, A., and Barbier, B. (2007) Order and anti-order in olivine III: variation of the cation distribution in the Fe,Mg olivine solid solution series with temperature and composition. European Journal of Mineralogy, 19, 15-27.
[11] Heuer, M. (2001) The determination of site occupancies using a new strategy in Rietveld refinements. Journal of applied crystallography, 34, 271-279.
[12] Hushur, A., Manghnani, M.H., Smyth, J.R., Nestola F., and Frost, D.J. (2009) Crystal chemistry of hydrous forsterite and its vibrational properties up to 41 GPa. American Mineralogist, 94, 751-760.

[13] Lager, G.A., Ross, F.K., Rotella, F.J., and Jorgensen, J.D. (1981) Neutron powder diffraction of Forsterite, Mg2SiO4: a comparison with single-crystal investigations. Journal of applied crystallography, 14, 137-139.
[14] Louisnathan, S.J., and Smith, J.V. (1968) Cell dimensions of olivine. Mineralogical Magazine, 36, 1123-1134.
[15] Matsui, Y., and Syono, Y. (1968) Unit cell dimensions of some synthetic olivine group solid solutions. Geochemical Journal, 2, 51-59.
[16] McCormick, T.C., Smyth, J.R., and Lofgren, G.E. (1987) Site occupancies of minor elements in synthetic olivines as determined by channeling-enhanced X-ray emission. Physics and Chemistry of Minerals, 14, 368-372.
[17] Merli, M., Oberti, R., Caucia, F., and Ungaretti, L. (2001) Determination of site population in olivine: Warnings on X-ray data treatment and refinement. American Mineralogist, 86, 55-65.
[18] Müller-Sommer, M., Hock, R., and Kirfel, A. (1997) Rietveld refinement study of the cation distribution in (Co, Mg)-olivine solid solution. Physics and Chemistry of Minerals, 24, 17-23.
[19] Nord, A.G., Annersten, H., and Filippidis, A. (1982) The cation distribution in synthetic Mg-Fe-Ni olivines. American Mineralogist, 67, 1206-1211.
[20] RRUFF.info
[21] Schwab, R.G., and Kustner, D. (1977) Precise determination of lattice constants to establish X-ray determinative curves for synthetic olivines of the solid solution series forsterite-fayalite. Neues Jahrbuch für Mineralogie, Monatshefte, 5, 205-215.
[22] Smyth, J.R., and Hazen, R.M. (1973) The crystal structures of forsterite and hortonolite at several temperatures up to 900 C. American Mineralogist, 58, 588-593.
[23] Urusov, V.S., Lapina, I.V., Kabala, Yu.K., and Kravchuk, I.F. (1984) Isomorphism in the forsterite-tephrolite series. Geokhimiya, 7, 1047-1055.
[24] van der Wal, R.J., Vos, A., and Kirfel, A. (1987) Conflicting results for the deformation properties of Forsterite, Mg2SiO4. Acta Crystallographica B, 43, 132-143.
[25] Yamazaki, S., and Toraya, H. (1999) Rietveld refinement of site-occupancy parameters of Mg2-xMnxSiO4 using a new weight function in least-squares fitting. Journal of Applied Crystallography, 32, 51-59.